JOINT EUROPEAN TORUS JET

JET–P(93)34

M.G. von Hellermann, H.P. Summers

Active Beam Spectroscopy at JET

Active Beam Spectroscopy at JET

M.G. von Hellermann, H.P. Summers[1]

JET-Joint Undertaking, Culham Science Centre, OX14 3DB, Abingdon, UK

[1]*Department of Physics and Applied Physics, University of Strathclyde, Glasgow.*

Preprint of a paper to be submitted for publication in a book published by
Elsevier Publishing Co. 'Atomic and Molecular Data for Fusion Reactor Technology'
May 1993

Active Beam Spectroscopy at JET

M.G. von Hellermann and H.P. Summers*)

JET Joint Undertaking, Abingdon OX14 3EA, *Department of Physics and Applied Physics, University of Strathclyde, Glasgow G4 0NG

Abstract

The status of active beam spectroscopy at the JET tokamak is described and an overview is given of the main developments of charge exchange (CXRS) and beam emission spectroscopy (BES). The recent preliminary tritium experiment at JET, where CXRS has provided ion temperature and deuteron density profiles, and BES has given an account of the tritium beam Balmer Alpha emission, has been a test case for quantitative spectroscopy. Magnetic field studies based on the motional Stark effect have led to precise measurements of the toroidal field and its local changes caused by diamagnetic effects. Absolute measurements of alpha particle densities and reconstruction of anisotropic slowing-down distribution functions are demonstrated for the case of helium neutral beam injection. Feasibility studies for alpha particle detection by CXRS are extrapolated to future fusion devices. The progress in the quality of atomic data is also illustrated by successful modelling of cross-section effects on observed line shapes which allows the prediction of apparent Doppler shifts, Doppler widths and line intensities.

Introduction

The progress in fusion research over the last decades is not only measured by its successes on the way to controlled fusion - the triple fusion product of the deuteron density, the deuteron temperature and the energy confinement time is approaching break-even conditions in present experiments [1] - but also by the parallel development of novel diagnostic tools providing reliable and quantitative values of key plasma parameters. Of special note in this area has been the use of powerful neutral beam heating and of consequent active charge exchange spectroscopy [2 - 15] which has led to a revolution of spectroscopic techniques.
The primary feature of charge exchange recombination spectroscopy (CXRS) is the emission of radiation following charge capture by fully stripped plasma ions from neutral beam donors leading to a Doppler broadened and also Doppler shifted spectrum (Fig.1) which reflects local plasma conditions. Radial profiles of temperature and plasma rotation can be derived from the width and peak position of the observed spectra. The second feature occurring in CXRS is the

selective population of high quantum shells by the charge capture process leading to radiation at visible wavelengths in the subsequent cascade. This has led to a renaissance of visible spectroscopy in fusion plasmas together with its associated advantages of high spectral resolution, routine absolute calibration techniques, and also optical components which facilitate high radial resolution from accessible observation ports.

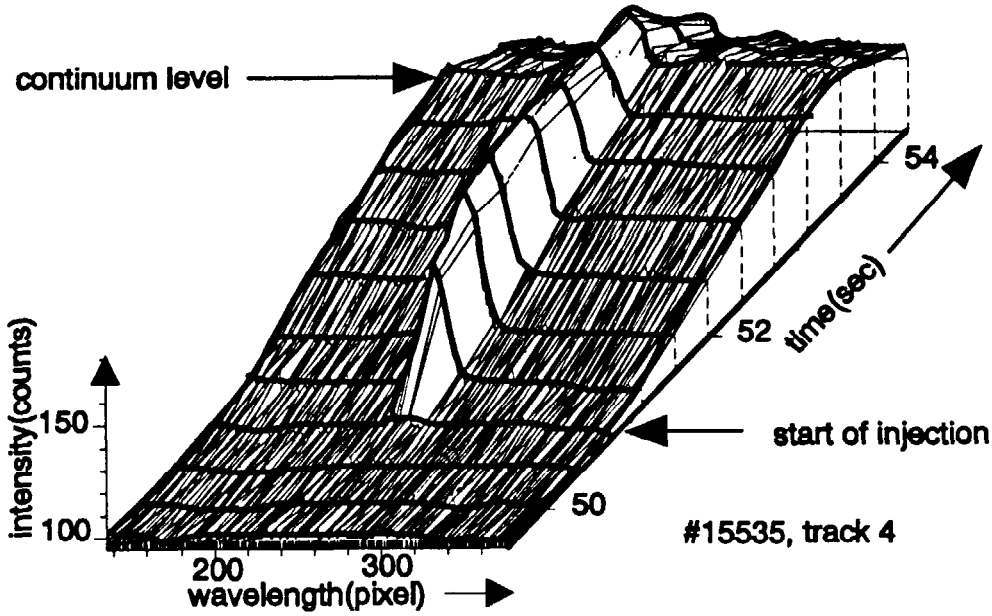

Fig.1 Demonstration of the principle of charge exchange spectroscopy with an example of fully stripped oxygen (n=10→9, λ=6068Å). No line radiation can be detected before beam injection, and a prompt signal occurs during injection. The intensity is a measure of local O^{8+} density, the spectral shift a measure of bulk plasma toroidal rotation and the Doppler width a measure of the plasma ion temperature. The continuum radiation level increases during injection primarily due to the increase in electron density during a H-mode phase.

A further attraction of active beam spectroscopy is the localisation of emission by optical lines of sight at points along a neutral beam line of well defined geometry and input power. Since there is now a refined understanding of the physics of beam plasma interactions causing beam attenuation such as ionisation and charge capture processes, local impurity densities can be deduced from absolutely calibrated spectral intensities, known emission rates, and calculated or measured local beam densities [11-15,23,24].

The modelled effective emission rates following charge capture take into account subsequent cascading and collisional redistribution processes. Their sensitivity to these implies that not only the collision energy (i.e. neutral beam energy) but also plasma density, plasma temperature and effective ion charge influence CX emission rates. Also beam stopping processes are a sensitive function of the target plasma impurity content and so an information of all impurities must be used for a consistent treatment. This is particularly the case for high electron densities where multiple collision processes need to be considered [15-18], and high levels of impurity concentrations (n_Z/n_e) affect non-linearly the beam attenuation in the plasma.

Complementing the wealth of diagnostic information offered by active charge exchange spectroscopy there is considerable additional diagnostic potential in the simultaneously

observed spectrum emitted by the high energy neutral beam atoms. From the first observations and initial quantitative interpretation, such as the Stark multiplet resolved in the intense Doppler shifted Balmer Alpha spectrum (cf. [19,20] and Fig.2), has stemmed beam emission spectroscopy (BES) and the development of a wide range of novel diagnostic techniques. These include ion density fluctuation measurements [21,22] and the direct determination of beam densities from absolute BES intensities [23,24], as well as the local measurement of the pitch angle of the internal magnetic field in a plasma and of the toroidal magnetic field based on the polarisation pattern of the Stark multiplet and its wavelength splitting respectively [23-27]. The Doppler shift of the entire multiplet allows the accurate determination of the position of the active observation volume, a valuable asset within in the complex collection of consistency checks of a diagnosed plasma. Due to the close connection between beam excitation processes and beam plasma processes, which determine beam attenuation, BES and CXRS are necessarily integrated in a fully consistent treatment.

In a JET plasma at thermo-nuclear conditions ($T_i \approx 20$keV) the bulk of the magnetically confined plasma is at temperatures above 2keV (cf. [28] and also table I). This implies that confined low-Z plasma ions are fully stripped and so do not emit discrete spectral lines. Only at the plasma edge there are lower ionisation stages, excited by collisions mostly with electrons, expected to contribute to line radiation. Nonetheless in the vicinity of the last closed magnetic flux surface line radiation from charge exchange processes between fully stripped ions and a population of neutrals in excited states is observed. The nature of this process is, that plasma ions are accelerated toward the wall and then reflected as neutrals (including $H^0(n=2)$) with energies substantially above thermal. This establishes the existence of an extended dense neutral layer and the possibility of multiple charge transfer processes, which may cause 'passive' i.e. non-beam related charge exchange recombination radiation. For example 'passive' CVI (n=8 to n=7, 5290Å) spectra (Fig.3) with a Doppler width corresponding to temperatures up to 4 keV are observed in low-density high-heating-power JET plasmas.

The interesting aspect of this observation is that 'active' beam spectroscopy, which is based on a charge transfer process between beam neutrals with velocities comparable to the bound electron orbit velocities, has led in the course of the last years also to a systematic extension of ion/atom cross-section studies into the lower energy region of charge exchange processes (< 10 keV/amu). In fact most of the known low-Z line radiation at the plasma edge is found to have comparable contributions from impact excitation and charge exchange processes. Small changes of the local neutral density have a strong impact on the population balance and thus radiated power [15,29].

The production and thermalising of thermo-nuclear fusion alpha particles and the control of the helium ash content are central topics in present and next-step fusion devices (cf. [30]). The experimental determination of the alpha particle distribution function, from birth energy down to thermal energies, and also related radial profiles, are therefore of considerable interest. Numerous active and passive diagnostic techniques in principle cover different parts of the energy spectrum, although with quite distinctive differences in their respective capabilities of energy resolution, spatial resolution and measurement of absolute particle numbers (c.f.[31]). JET has recently completed a comprehensive study of the atomic physics involved in active beam based charge exchange recombination spectroscopy of alpha particles [32]. In this paper some of the recent results reflecting the progress in the modelling of spectra and measurement of slowing-down features [33] are highlighted .

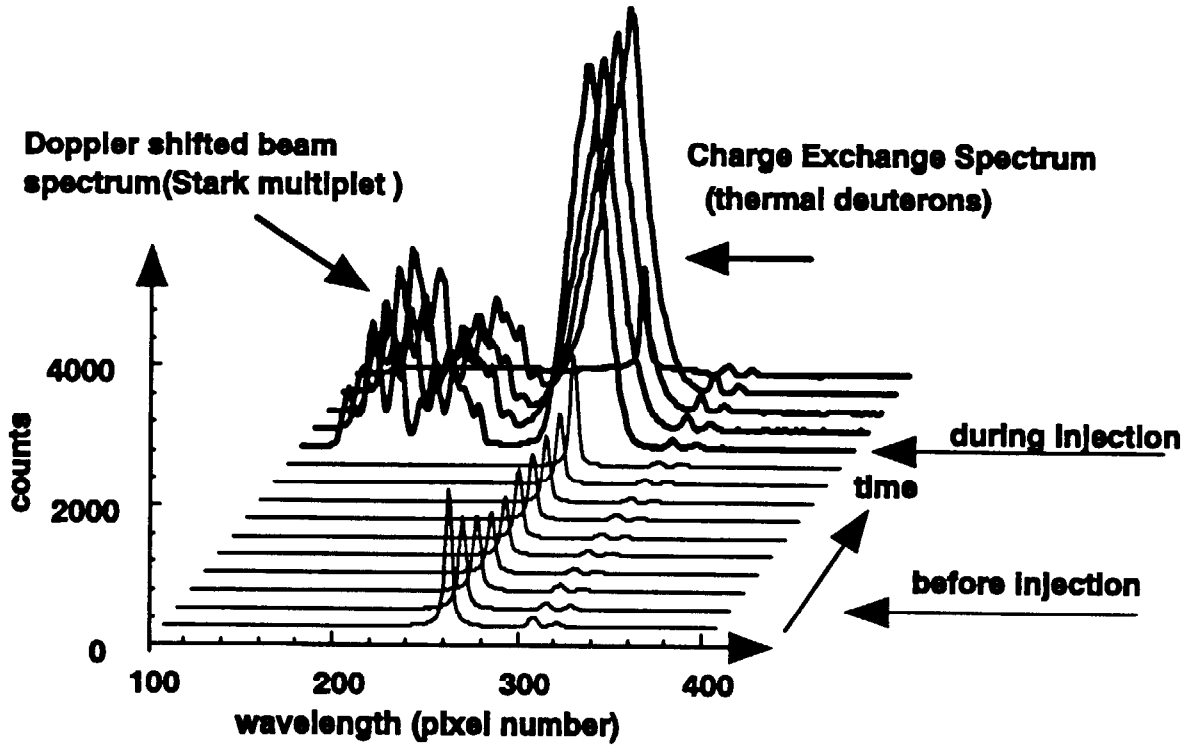

Fig.2 Composite emission of charge exchange features in the Balmer-Alpha spectrum and the Doppler shifted beam-emission spectrum showing the three energy components of the neutral deuterium beam and partially resolved details of the Stark multiplet.

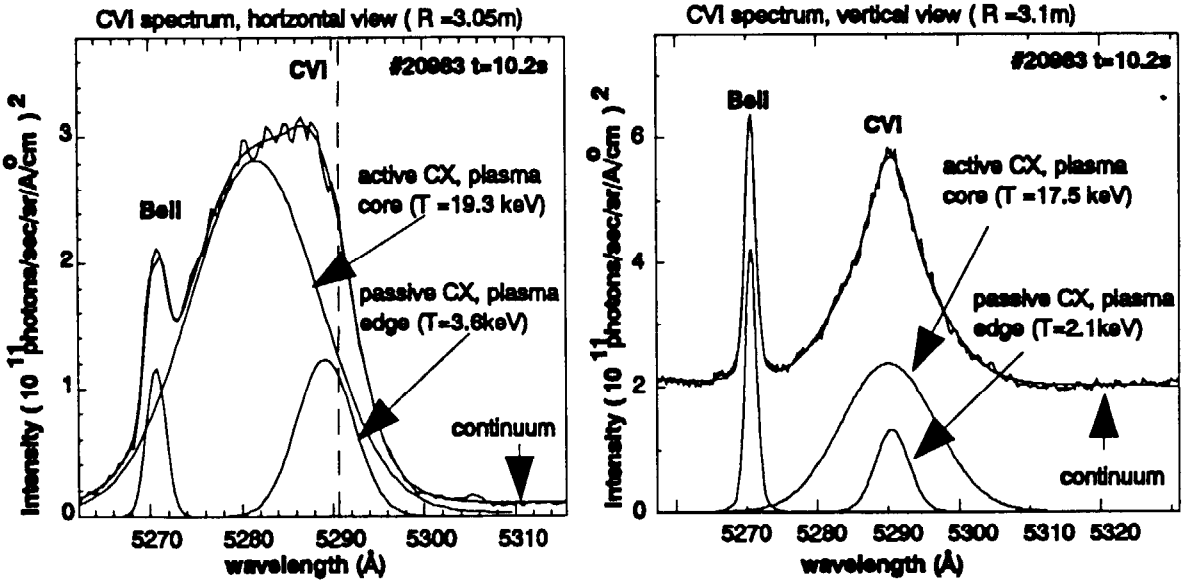

Fig.3 Charge exchange spectrum of CVI at 5290.5Å (T=19.3keV) from the active volume and its passive background spectrum (3.6 keV) emitted in the vicinity of the magnetic separatrix. Two spectra are shown: One representing a view from the top of the machine, and the second is one chord of the horizontal multi-chord system. The plasma is in a low-density high-power H-mode regime [28].

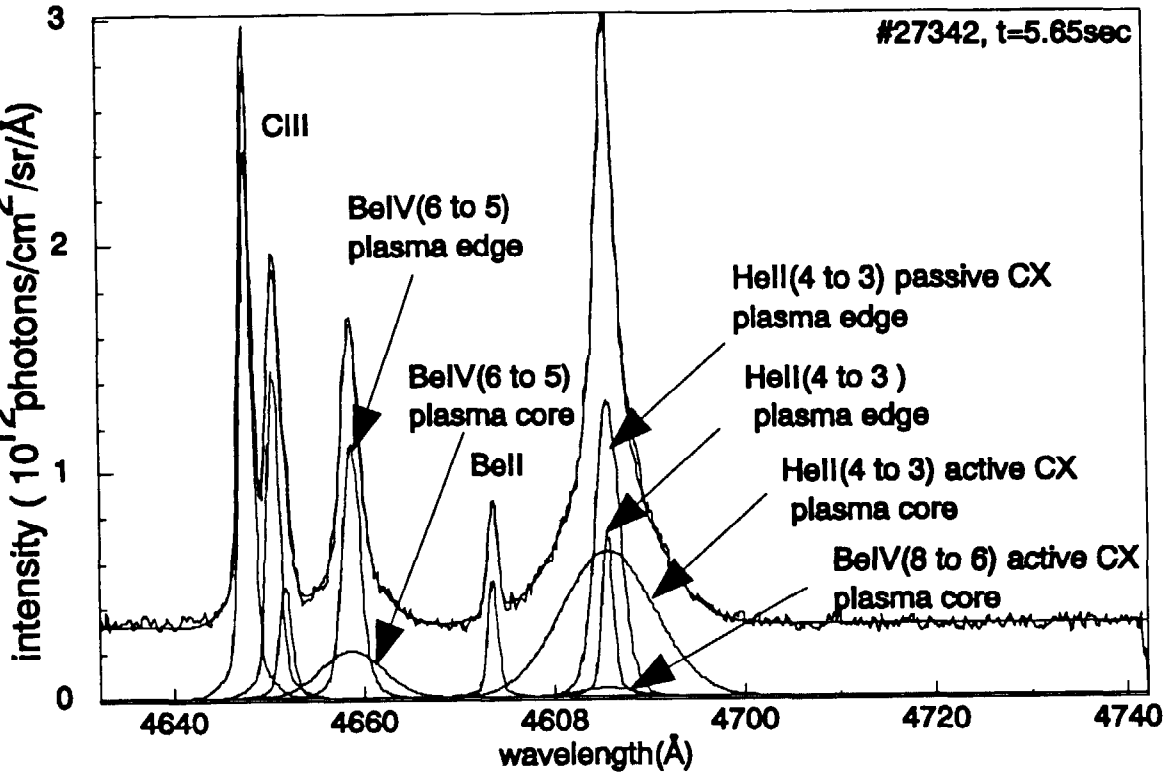

Fig.4 The HeII and BeIV CX spectra and the passive background line spectra of CIII and BeII [33,34]. In the multi-gaussian resolution shown, a fixed intensity ratio (5:3:1) is assumed for the CIII triplet. The BeIV and HeII CX components are assumed to have equal temperatures. The ratio of the two BeIV CX lines is 5.2 [29]. Zeeman splitting of the CIII and BeII lines is not resolved.

Experimental

The central plasma, vertical JET CXRS diagnostic comprises two spectrometers for the simultaneous measurement of the visible CX transitions of the plasma impurities carbon, beryllium and helium and their respective temperatures and densities in the plasma centre. This single line of sight from the top of the vessel shares an entrance window with an UV fibre-less optical link to remote instruments located in the roof laboratory above the JET torus hall [35]. In addition, two multi-chord systems sharing an observation port in the torus mid-plane are used for horizontal CXRS and BES respectively (Fig.5). The instruments are located beyond a biological shield and the light is transferred via quartz fibres. Each spectrometer is equipped with a 2-dimensional CCD camera. Typical readout times are 50 msec for the multi-chord, and 5 msec for the single-chord systems respectively. Temperature and rotation velocity profiles are usually derived from CVI (Fig.3) spectra, except in helium fuelling experiments where helium represents the main impurity and the HeII CX spectrum is used.

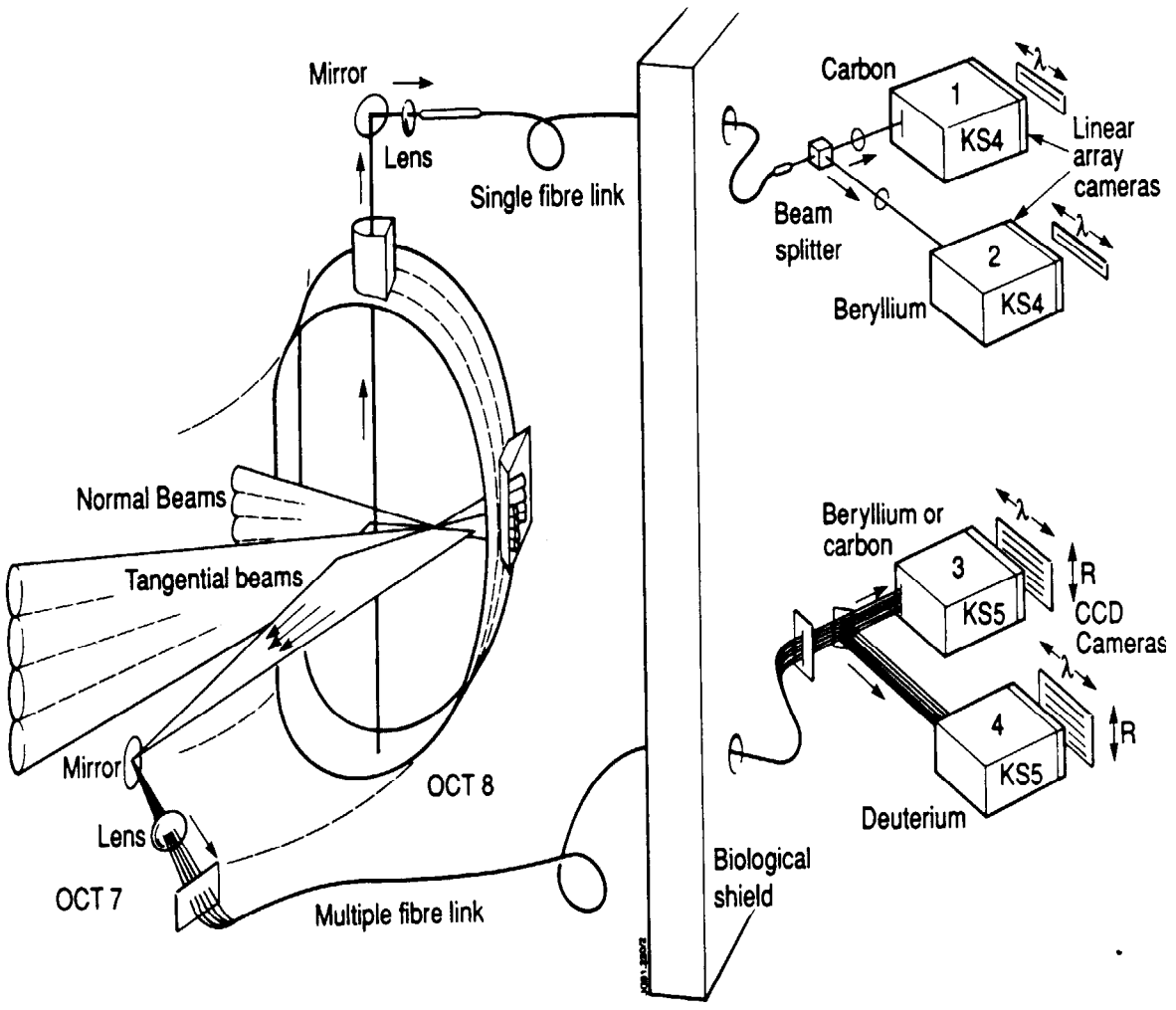

Fig.5 The JET CXRS and BES diagnostic showing four of its spectrometers equipped with 2-dimensional CCD cameras. The BES multi-chord system measures the intensities in two perpendicular directions of polarisation from the same plasma location using beam-splitter polarisers in front of the fibres [24,45].

Spectral analysis procedures

In spite of the advances in the deduction of densities, temperatures, rotation speeds etc. from CX spectra, it is the actual spectral analysis, which still represents a restriction in moving to real time analysis. The decomposition into multi Gaussian components involves time consuming interactive procedures. There is a wide range in the complexity of spectra as illustrated by the examples shown in Fig.1 to Fig.4, and also in Figs. 13, 22, and 24, 26. Significant acceleration and enhanced reliability was achieved at JET by the introduction of

coupled-parameter fit techniques [23,24,34]. Atomic physics data such as known wavelength separations or constant intensity ratios and input from plasma physics such as equal ion temperatures for the low-Z impurities can be imposed to reduce the number of free parameters. In the HeII/BeIV spectrum (Fig.4, Fig.22, Fig.24) for example, a fixed intensity ratio 5:3:1 for the CIII triplet is used. Also for the two BeIV CX lines at λ=4658.55Å and λ=4685.25Å respectively, the ratio of the emission rates $\sigma v_{CX}(n=6\rightarrow5):\sigma v_{CX}(n=8\rightarrow6)=5.2$, which had been established experimentally and theoretically, is applied. New developments in neural network approaches [36] promise further significant reduction in computing time by using neural network solutions as initial estimates for the standard least square routines. A fully automatic analysis for most of the known CX spectra appears however not to be realistic in view of the wide dynamic range of background spectral intensities, the variety of plasma operation schemes and also the changing role of wall materials.

Deduction of deuteron density profiles

The reconstruction of radial deuteron density profiles and of effective ion charge profiles:

$$Z_{eff}(r) = 1 + \sum_z Z_z (Z_z - 1)\frac{n_z(r)}{n_e(r)} \qquad (1)$$

$$n_d(r) = n_e(r) - \sum_z Z_z n_z(r) \qquad (2)$$

where Z_Z and n_Z are charge and density of impurity ion z, and n_e, n_d are electron density and deuteron density, is based on charge neutrality and the assumption that the central values of the three main impurities (C, Be and He) may be used as a constant ratio throughout the profile. This procedure is probably justified for the description of intrinsic impurities, but strictly speaking all three radial impurity profiles should be assessed independently for a consistent treatment of the attenuation process, and also for the derivation of plasma transport data. In particular in high power helium fuelling experiments it is found that fuelled particle profiles may differ from that of intrinsic impurities [33].

It should be noted that for the majority of plasmas, with low impurity content, the uncertainty of deriving a local deuteron density via equation (2) is lower than the direct determination of n_d from a CXRS measurement of the Balmer-Alpha spectrum (cf. [23,24]). This is mostly due to beam halo effects which lead to the greatest uncertainty in the interpretation of the Balmer-Alpha CX spectrum. Assuming an overall error of the order of 30% for the absolute measurement of the intrinsic impurities C, Be and He, the indirect calculation of the plasma dilution $d = n_d/n_e$ will be still quite reliable. The relative dilution error caused by an uncertainty in low-Z impurity concentrations can be written as:

$$\frac{\delta d}{d} = \frac{1-d}{d}\frac{\delta c}{c} \qquad (3)$$

where $\delta c/c$ is the relative error in deduced impurity concentration $c=n_z/n_e$. That is for a dilution factor of the order d=0.9 the estimated relative error is only 3 %. By comparison, if $c_d = n_d/n_e$ had been used, the minimum uncertainty would have been at least 30 %.

Absolute calibration and geometry factors

The JET CXRS instruments are calibrated using tungsten lamp calibration sources. In addition there is a routine cross-calibration option provided by the underlying bremsstrahlung continuum. This practice is in fact indispensable for optical heads, in-vessel mirrors and windows close to the plasma boundary, whose transmission factors deteriorate in the course of operation. On the other hand some of the entrance windows, which are used by the visible spectroscopy diagnostics at JET, are remote from plasma contamination sources and provide therefore stable calibration values for a cross-reference on the measured continuum radiation level. The bremsstrahlung photon flux may me expressed as:

$$\Phi_{brems}\Delta\lambda = B \cdot g_{ff} \cdot < Z_{eff} > \int dr \cdot n_e^2(e) \frac{\Delta\lambda}{\lambda_{de}(r)} \qquad (4)$$

where $B = \left[\frac{e^2}{4\pi\varepsilon_0}\right]^3 \frac{16}{3hc^4 m_e^2}\sqrt{\frac{\pi}{3}}$, $\lambda_{de}(r) = \frac{\lambda}{c}\sqrt{\frac{2T_e(r)}{m_e}}$ and g_{ff} is the free-free Gaunt factor.

The equivalent Doppler width λ_{de} has been introduced for a comparison with the active CX photon flux (5) and also the discussion of signal-to-noise ratio (cf. the section detection limits of this paper). G_{ff} is the free-free Gaunt factor, and $<Z_{eff}>$ the line-of-sight averaged effective plasma ion charge. Since each of the CX instruments is viewing the same plasma at the same time we compare their respective continuum radiation signals by an appropriate mapping onto equivalent magnetic flux surfaces.

The CX spectral intensity is given by:

$$\Phi_{cx}(\lambda)\Delta\lambda = \frac{1}{4\pi} n_z \cdot \frac{\Delta\lambda}{\sqrt{\pi}\lambda_{di}} \exp\left\{-(\lambda-\lambda_o)^2/\lambda_{di}^2\right\} \sum_E < \sigma v(E) >_{cx} \int n_b(E,s) ds \qquad (5)$$

The integral with respect to ds, with ds=ds(x,y,z), is along a line-of-sight integration across the neutral beam profile. The latter may be described by a Gaussian profile:

$$n_b(x,y,z) = \frac{P}{eEv_b} \frac{1}{\pi w_x(z) w_y(z)} \exp\left\{-\frac{x^2}{w_x^2(z)} - \frac{y^2}{w_y^2(z)}\right\} \qquad (6)$$

The beam co-ordinate system used here is defined with its z-axis along the neutral beam, and the x- and y-co-ordinates perpendicular to the beam. P, E, and v_b denote local beam power, energy and velocity respectively. In JET eight individual neutral beams with - in principle - different power levels, energies, species mixes, fuelling gases, beam divergences etc. may contribute to an observed spectrum. For the JET neutral beam assembly geometrical factors, including beam alignment, beam divergence and precise orientations of viewing lines, have a substantial impact on deduced absolute impurity levels. Extensive cross-calibration procedures are necessary. For this reason dedicated neutral beam pulses, where each individual beam is controlled separately, are used to confirm the actual geometry and the geometrical contribution from each beam.

Iterative deduction of impurity densities

The deduction of absolute impurity densities (equation (5), (6) and (7))from measured absolute spectral intensities and calculated neutral beam densities is achieved by an iterative procedure since the calculated local beam density (equation (8)) depends on the stopping cross-sections and - in principle - also on radial concentration profiles $c_z(r) = n_z(r)/n_e(r)$ of the investigated impurities. The procedure is to start from an initial approximate impurity level, obtained usually from visible bremsstrahlung (equation (1) and (4)), and reenter the impurity density resulting from the CX evaluation into the next iteration of attenuation calculation. The deduced impurity density is:

$$n_z = \frac{4\pi \int \Phi_{cx}(\lambda) d\lambda}{n_b L_{cx} \langle \sigma v \rangle_{cx}} \qquad (7)$$

Where $\Phi_{cx}(\lambda)$ is the absolutely calibrated CX photon flux, $n_b L_{cx}$ the line integrated beam density at the observation volume, and $\langle \sigma v \rangle_{cx}$ the effective emission rate. The local beam density is related to the vacuum beam density by:

$$n_b = n_b(0) \exp\left\{ -\int dl \cdot n_e(l) \sum_z \sigma_{sz} c_z(l) \right\} \qquad (8)$$

The integration dl=dl(r) is along the neutral beam path from plasma boundary to observation volume. Precise electron density profile data $n_e(r)$, and effective beam stopping cross-sections σ_{SZ} are essential for the reliability of calculated neutral densities. The exponential attenuation amplifies the sensitivity to errors, and becomes more critical as the density increases and multiple step processes become involved. The second implication of this procedure is that *all* impurities need to be taken into account. The actual iteration procedure in use at JET converges usually within one or two iterations and a unique solution is obtainable. The usual procedure is to start with the dominant impurity and then include the remaining low-Z impurities.

Cross-section effects on observed line shapes

An important aspect of the CXRS diagnostic of high temperature fusion plasma is the recognition that detailed shapes of ion/atom cross-sections especially local gradients and curvature of the effective emission rate coefficient nearby the beam energy (cf. Fig.6) influence observed spectra. These effects must be taken into account in routine data analysis procedures. For hot fusion plasmas with thermal velocities comparable to the beam velocity the range of individual collision energies in the centre of mass frame can vary substantially and hence the shape of the observed CX spectrum is affected by the variation of the effective emission rate coefficient. The effects of collision energy dependent cross-sections on observed CX spectra have been described previously in several papers, in particular for thermal spectra of UV CX lines [37], for thermal and non-thermal low-Z impurity spectra with CX transitions in the

visible spectral range [38,14,39], and for observations of fast ion density radial profiles in helium beam fuelling experiments [33]. In the case of a thermal distribution function the calculated modified spectrum is approximated by a Gaussian whose Maxwellian width, peak position, and intensity defines an 'apparent temperature', an 'apparent velocity' and an 'apparent intensity'. The calculation involves for each individual case the consideration of the specific observation geometry including the angle between line-of-sight and neutral beam, and for the case of toroidal plasma rotation, the angle between line-of-sight and toroidal direction. The observed spectrum in the observation direction z, is described by:

$$f(v_z) = \iiint dv'_x\, dv'_y\, dv'_z Q(v_{col})\delta(v_z - v'_z) g(v'_x, v'_y, v'_z) \tag{9}$$

$$g(v_x, v_y, v_z) = \frac{1}{a^3 \pi^{3/2}} \exp\left\{ -\frac{v_x^2 + v_y^2 + v_z^2}{a^2} \right\} \tag{10}$$

where g(v) is the three-dimensional thermal velocity distribution function, a the thermal velocity, $Q(v_{col})=\sigma(v_{col})v_{col}$ the effective emission rate coefficient, v_{col} the collision velocity, and z is the direction of observation. The neutral beam is in the y-z-plane of the observation co-ordinate system (cf.[33]), with the angle δ between neutral beam and y-axis. The nature of the cross-section effect can be illustrated by an analytical model (cf. [40]), which explains the effects of local gradients:

$$\alpha' = \frac{1}{Q}\frac{\partial Q}{\partial v} \text{ and curvatures } \beta' = \frac{1}{Q}\frac{\partial^2 Q}{\partial v^2} \tag{11}$$

on 'apparent velocities', 'apparent temperatures', and mean emission rate coefficients averaged over the target velocity distribution function. In this paper the main results are briefly summarised. The central assumption of the model is, that the emission rate $Q=\sigma(v_{col})\cdot v_{col}$ may be presented as an exponential expression with only first and second order velocity terms in its exponent. The integral (9) can then be performed analytically. We write:

$$Q_{cx} = Q_{cx,0} \exp\left[\alpha(v_{col} - v_b) + \beta(v_{col} - v_b)^2\right] \tag{12}$$

where α and β are related to α' and β' by :

$$\alpha = \alpha'; \beta = \frac{1}{2}(\beta' - \alpha'^2) \tag{13}$$

The analytic solution of (9) implies an effective velocity distribution function with apparent velocity and temperature:

$$v_{app} = \frac{\alpha \sin\delta \cdot a^2}{2(1 - a^2\beta)} \tag{14}$$

$$T_{app} = T\frac{1-a^2\cdot\cos^2\delta\cdot\beta}{1-a^2\cdot\beta} \qquad (15)$$

The effective emission rate, averaged over the velocity distribution function is:

$$<Q>= Q_0\frac{\exp\left[\frac{\alpha^2a^2}{4(1-a^2\beta)}\right]}{\sqrt{1-a^2\beta}} \qquad (16)$$

The set of equations (14, (15, (16) and also Fig.6 illustrate the main features of the cross-section effect. The apparent Doppler shift $\Delta\lambda = -\frac{v_{app}}{c}\lambda_0$ of the observed spectrum is proportional to the gradient α, viewing angle $\sin\delta$ and to the temperature T which is proportional to a^2. For an injection energy beyond the maximum of Q_{cx} (cf. Fig.6), i.e. $\alpha<0$, an apparent blue shift arises and for an injection energy below the maximum, i.e. $\alpha>0$, a red-shift. The negative values of 'curvature' β (cf. Fig.6c) for the main part of Q_{cx} , implies that in general the collision energy dependent excitation rate leads to an apparent temperature *less* than the true temperature.

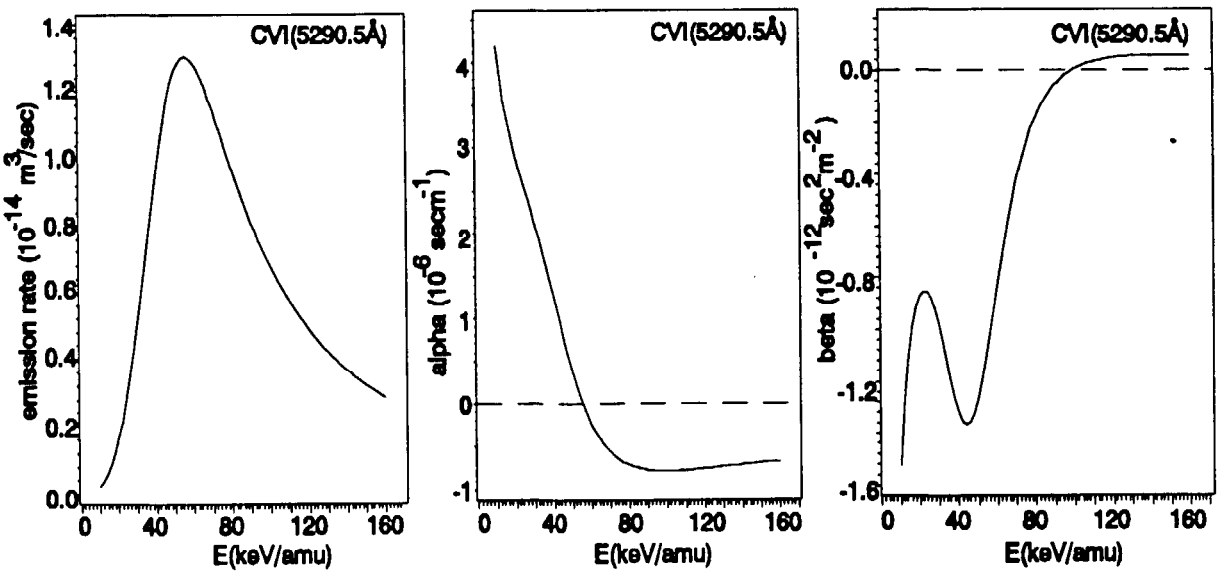

Fig.6 a) Emission rate coefficient for the CVI transition (n=8→7) and its shape parameters versus collision energy. The data points have been calculated for a 'standard' plasma of Z_{eff}=2, T = 5 keV, n_e =$3\cdot10^{19}m^{-3}$ [cf.11]. b) 'gradient' α of the emission rate curve c) 'curvature' $\beta = 0.5(\beta'-\alpha^2)$.

A CXRS test case - the JET Preliminary Tritium Experiment

One of the greatest challenges at a major fusion experiment such as the JET tokamak is the task of ensuring the consistency of data. On the other hand, a great asset at JET is the large number of independent diagnostic systems employing markedly different techniques measuring overlapping or complementary plasma data. For example, the measured neutron yield in a D-T plasma, and its consistency with the main measured plasma parameters, are intensively scrutinised. Accurately measured ion temperature profiles and deuteron density profiles are key ingredients for codes [41] simulating the actual beam-beam, beam-thermal and thermal-thermal neutron production. Some CXRS results of the JET *'preliminary tritium experiments'* PTE (cf. [1]) are presented in this section. The four selected pulses are, a reference discharge (#26087) where the so far highest fusion yield equivalent was achieved, (#26095) a further reference pulse with a 1% tritium content, and the actual PTE pulses (#26147 and #26148) with a tritium:deuterium ratio of 0.13. Table I gives an overview of the main CXRS data. The three impurities He, Be and C are used in a self consistent calculation of the neutral beam attenuation and for the deduction of deuteron density and $Z_{eff}(0)$. The line averaged values of $<Z_{eff}>$ refer to dedicated visible bremsstrahlung measurements and the equivalent values measured by the CXRS diagnostic are based on complete radial profiles (cf. equation (4) and (1) respectively). The central values of Z_{eff} agree within their respective error bars with the line averaged results of visible bremsstrahlung indicating a flat Z_{eff} profile.
In PTE pulse #26148 tritium was injected into a deuterium target plasma by two of the sixteen JET neutral injectors using tritium as fuelling gas. The time evolution of neutral beam power, including that of the tritium beams, the total d-t neutron rate and the projected thermal d-t rate, central ion and electron temperatures, and the densities of the main low-Z impurities densities are shown in Fig.7. It should be noted that for this pulse three different types of neutral beams contribute to the collected CX spectra. There were four deuterium beams at 140 keV, two deuterium beams at 80 keV and two tritium beams at 80keV. The complex Balmer-Alpha beam emission spectrum and the peaks due to full, half and third energy components of the tritium beam are shown in Fig.9. The tritium fuelling phase at low power is in parallel with the actual heating phase where the ion temperature profile (Fig.8) is built up reaching a peak value of 19 keV. The volume integrated thermal-thermal neutron reaction rate $Y_{d\text{-}d}$ has been derived from the deuteron density profile (equation (2)) and the thermal d-d and d-t reaction rates (as quoted in [42]) as a function of the ion temperature profile.

$$Y_{d-d} = \frac{1}{2}\int dV(\psi)\cdot n_d^2(\psi) < \sigma v_{d-d}(\psi) > \qquad (17)$$

ψ is the magnetic flux surface index and $dV(\psi)$ the corresponding volume element. Both $T_i(r)$ and $n_d(r)$ are symmetrised about the magnetic axis. A further example of the consistency checks is given in Fig.10, where TRANSP [41] calculations of the thermal-thermal neutron rate are shown together with the rates derived directly from the CXRS profiles. The experimental uncertainties in ion temperature and deuteron densities are reflected in the upper and lower values and indicate the general consistency. In Fig.11 we show the tomographic reconstruction of the central neutron emissivity as measured by the JET neutron profile monitor [43] and a comparison with the thermal-thermal emissivity based on CXRS data. It is

interesting to note, that both the central total neutron emissivity and the thermal-thermal emissivity curves flatten off well in advance of the final 'crash' of the total, volume integrated rate, which is caused by the influx of impurities.

table I

pulse	#26147	#26148	#26095	#26087
time	13.12	13.21	13.7	13.4
n_t/n_d	0.13	0.13	0.01	0.0
$T_i(\psi=0)$ keV	17.50±0.60	18.80±0.80	20.70±1.00	18.60±0.9
$T_i(\psi=1)$ keV	3.30±0.10	5.20±0.10	3.10±0.10	3.90±0.1
$c_C(\%)$	2.70±0.40	3.00±0.35	2.10±0.35	1.90±0.30
$c_{Be}(\%)$	1.25±0.25	1.25±0.25	0.70±0.17	0.75±0.20
$c_{He}(\%)$	1.75±0.35	0.60±0.25	1.20±0.30	1.40±0.40
$n_d(r=0)10^{19}m^{-3}$	2.30±0.15	2.10±0.15	4.30±0.20	3.90±0.18
$Z_{eff.CX}(r=0)$	2.00±0.25	2.05±0.25	1.85±0.27	1.80±0.25
$\langle Z_{eff.CX}\rangle$	2.15±0.25	2.00±0.20	1.95±0.25	1.75±0.25
$\langle Z_{eff.vis\text{-}brems}\rangle$	2.15±0.30	2.20±0.30	1.98±0.30	1.70±0.25
$Y_{d\text{-}d}$(thermal)$10^{16}s^{-1}$ CXRS	0.90±0.10	1.10±0.15	2.10±0.40	2.30±0.30
$Y_{d\text{-}d}$(thermal)$10^{16}s^{-1}$ TRANSP	0.75	0.85	1.88	2.5

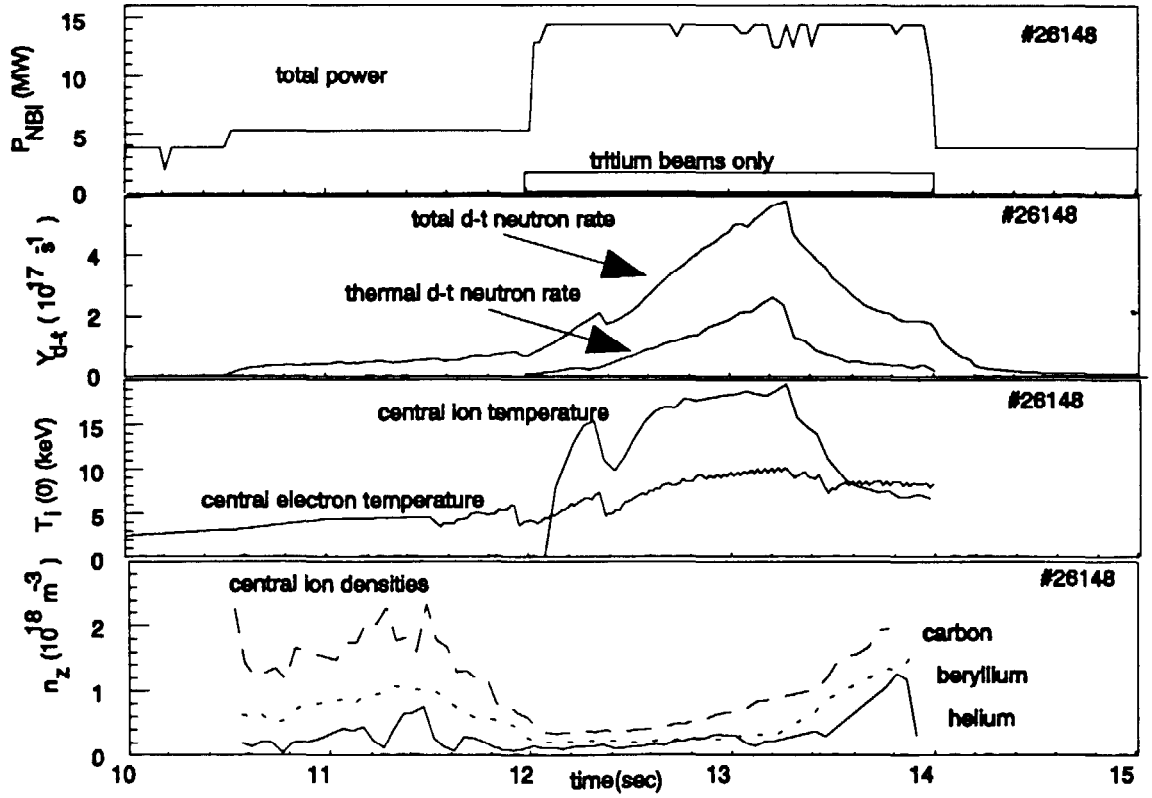

Fig.7 Temporal evolution of the main parameters in PTE pulse #26148. Total NB power, the tritium fuelling power is shown as an inlet. b) Total neutron rate, and the projected thermal-thermal d-t rate deduced from CX data. c) Central ion and electron temperatures. d) Central densities of the main light impurities. The high fusion yield phase is terminated by an influx of impurities at 13.4 sec.

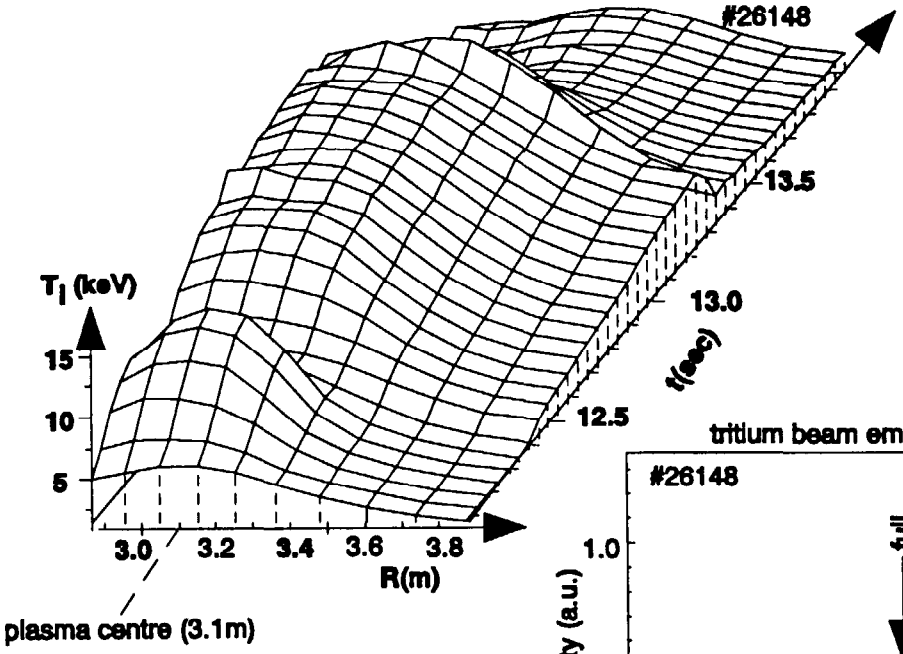

Fig.8 PTE ion temperature profile. A low-power tritium beam fuelling phase precedes the actual NBI heating phase (15 MW).

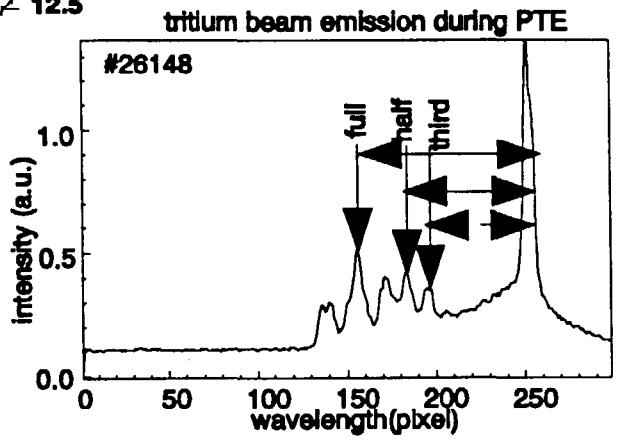

Fig.9 Beam-emission spectrum of D- and T-beams. The 3 energy species of the T beams are indicated.

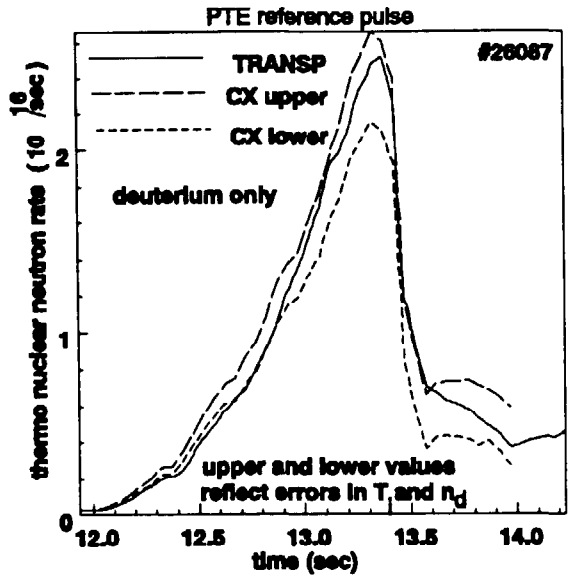

Fig.10 Thermal neutron yield in reference pulse #26148 calculated by the JET TRANSP code and comparison with data deduced from the CXRS diagnostic.

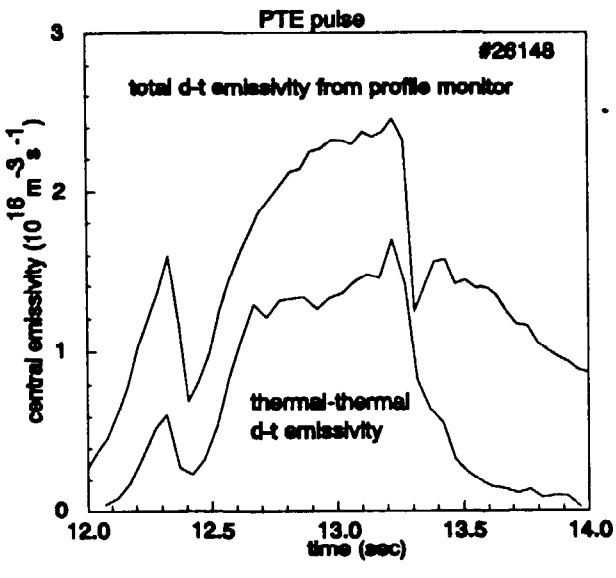

Fig.11 Central neutron emissivity reconstructed from neutron profile monitor data [43] and emissivity calculated from $\sigma_{d\text{-}t}(T_i)$, n_d and n_d:n_t ratio.

Beam Emission Spectroscopy

Balmer Alpha Beam emission spectroscopy [23,24] allows a direct measurement of the local neutral beam density. The two dominant excitation processes leading to the Doppler shifted beam emission spectrum (Fig.13) are electron and ion impact:

$$D^0 + A^z \rightarrow D^{0,*} + A^z \qquad \text{(ion impact)} \qquad (18)$$

$$D^0 + e^- \rightarrow D^{0,*} + e^- \qquad \text{(electron impact)} \qquad (19)$$

By collisional radiative modelling [15] of the excitation processes the calibrated intensities can be used to reconstruct local beam densities (Fig.14) and establish the species mix (Fig.15). The results achieved so far [23,24] have demonstrated the necessity of high quality plasma input data, such as electron density and temperature profiles, Z_{eff} profiles, and also precise beam geometry data. Since a Z_{eff}-profile is the outcome of CXRS on light impurities the argument can be reversed: The analysis of BES data offers an additional consistency check and should be treated as an inseparable part of a comprehensive CXRS analysis. A further interesting application is the use of ratios of line intensities in the combined CXRS and BES D-alpha spectrum and their respective atomic emission rates, to deduce Z_{eff} profiles independent of absolute calibrations [23,24].

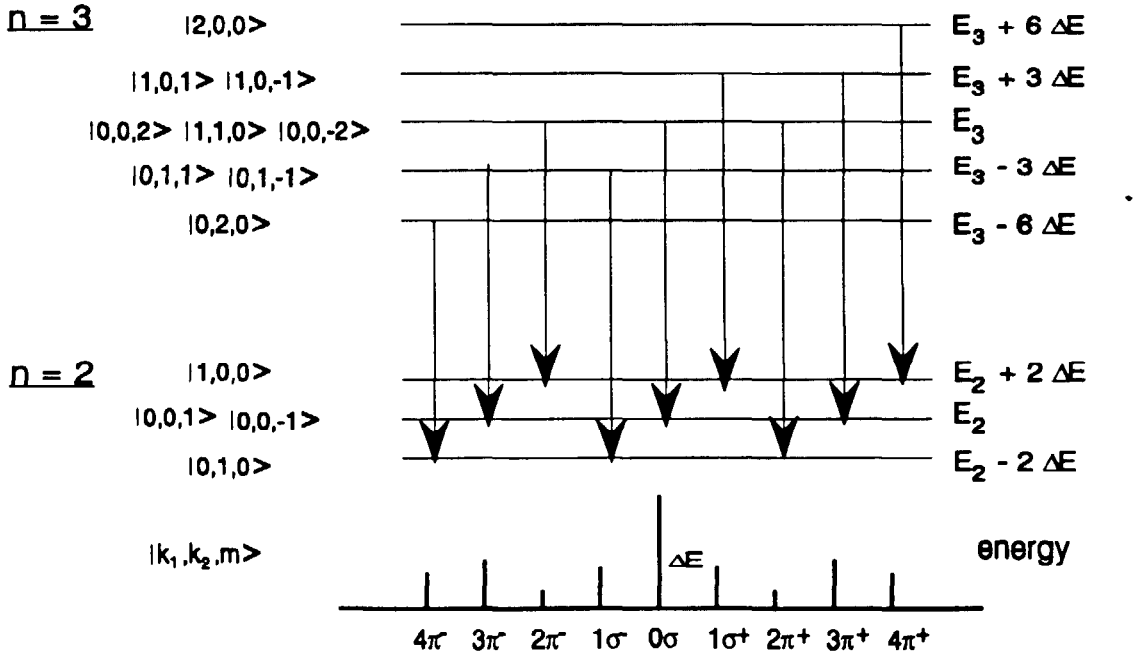

Fig.12 Energy term diagram for the linear Stark effect on the D_α/H_α-transition. The schematic spectrum, for observation at 90° to the Lorentz field, shows the symmetry of the Stark multiplet which is used in the coupled fit (Fig.13) (see also [45]).

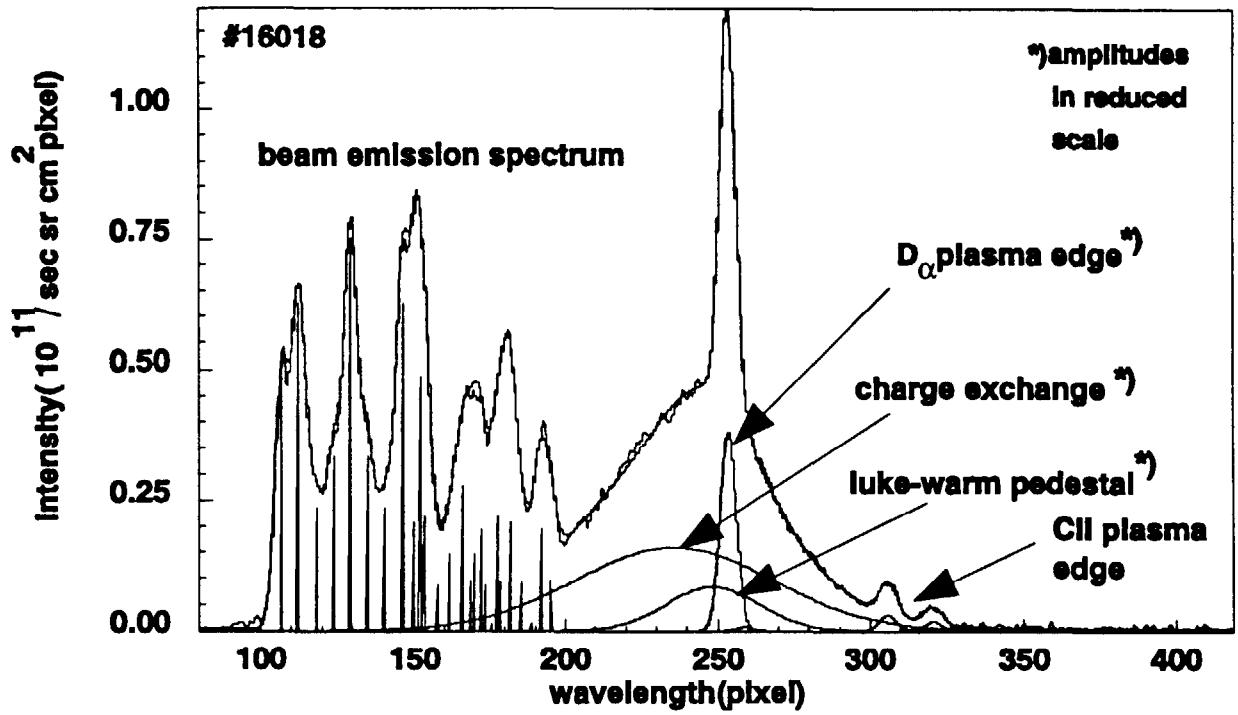

Fig.13 Balmer-Alpha CXRS and BES spectrum. The Stark multiplet components are indicated by their positions and respective heights. The amplitudes of the Gaussian fit profiles for edge, pedestal and CX features are reduced in scale by a factor 2 for clarity[cf. 23,24] .

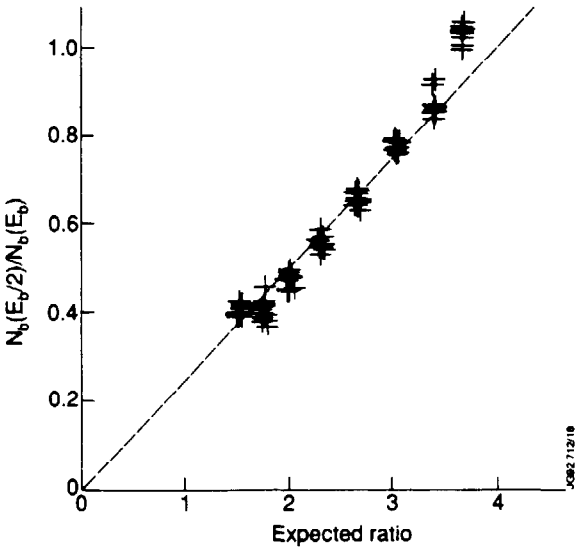

Fig.14 Comparison of beam densities deduced from collisional radiative modelling of the BES intensity with calculated densities using beam stopping cross-sections [23,24]

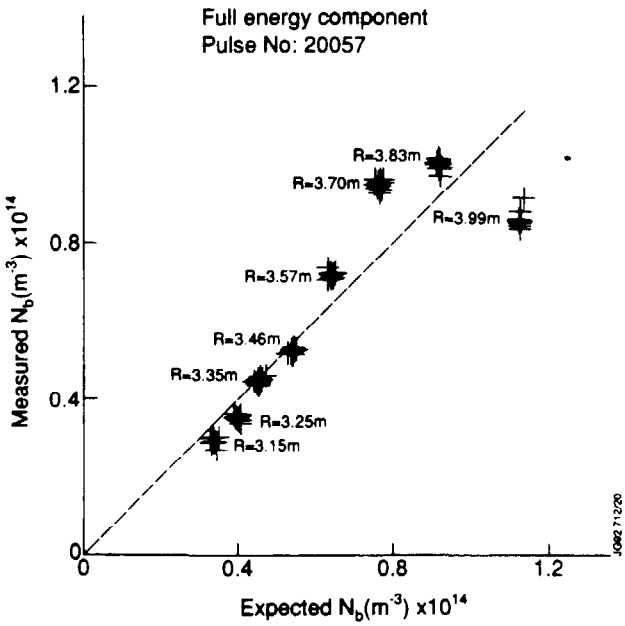

Fig.15 Density ratio of E/2 to full energy E deduced from BES data and comparison with calculated ratios assuming an equal species mix.

The polarisation pattern of the motional Stark features (MS) contains information on the magnetic field direction while the Stark wavelength splitting is essentially a measure of the toroidal magnetic field component. Fig.16 shows the orientation of the Lorentz field vector **E=vxB** and the array of possible magnetic field vectors in the plane perpendicular to **E** and beam velocity **v** which give the same electric field strength. Usually the Stark pattern is measured close to the magnetic mid-plane and the magnetic field which is defined by its toroidal and poloidal components can be unambiguously determined by two components only. The JET BES/MS diagnostic uses 4 pairs of fibres each measuring a spectrally resolved Stark multiplet in two perpendicular directions of polarisation. Fig.17 shows schematically the optical head with its half-wave plate and polarising beam-splitter cubes which split the light of one radial position into two polarisation channels. The simultaneous measurement of pitch-angle and Lorentz field strength enables the deduction of both local poloidal and toroidal magnetic fields. The present experimental equipment at JET is capable of resolving polarisation angles of the order 0.2°. A further strength of internal magnetic field measurements at JET is the unique combination of Motional-Stark and Faraday-Rotation techniques. In dedicated experiments with circular magnetic flux surfaces the on-axis value of the safety factor $q(0)<1$ was confirmed by the two diagnostics [27]. Sweeping of the magnetic axis leading to an enhanced spatial resolution - both diagnostics have only a few radial channels - has enabled sensitive pitch angle measurements at the magnetic axis (Fig.18).

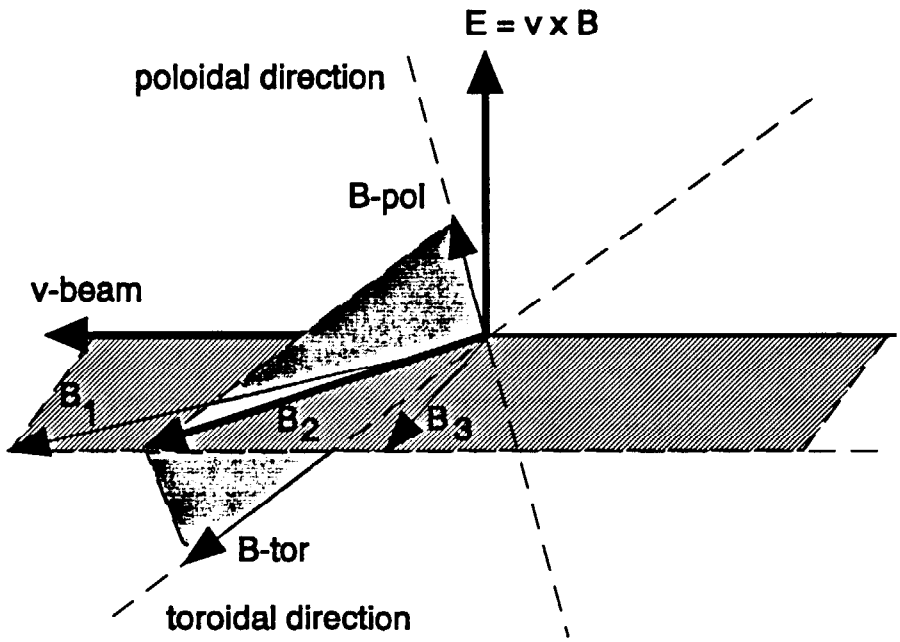

Fig.16 The polarisation pattern and wavelength splitting determine the orientation and strength of the Lorentz field vector. All B-vectors B_1, B_2 and B_3 indicated in this figure lead to the same Lorentz vector. Only in the magnetic mid-plane both the toroidal and poloidal field direction are known and the total magnetic field can be uniquely determined by a combined polarisation and wavelength measurement.

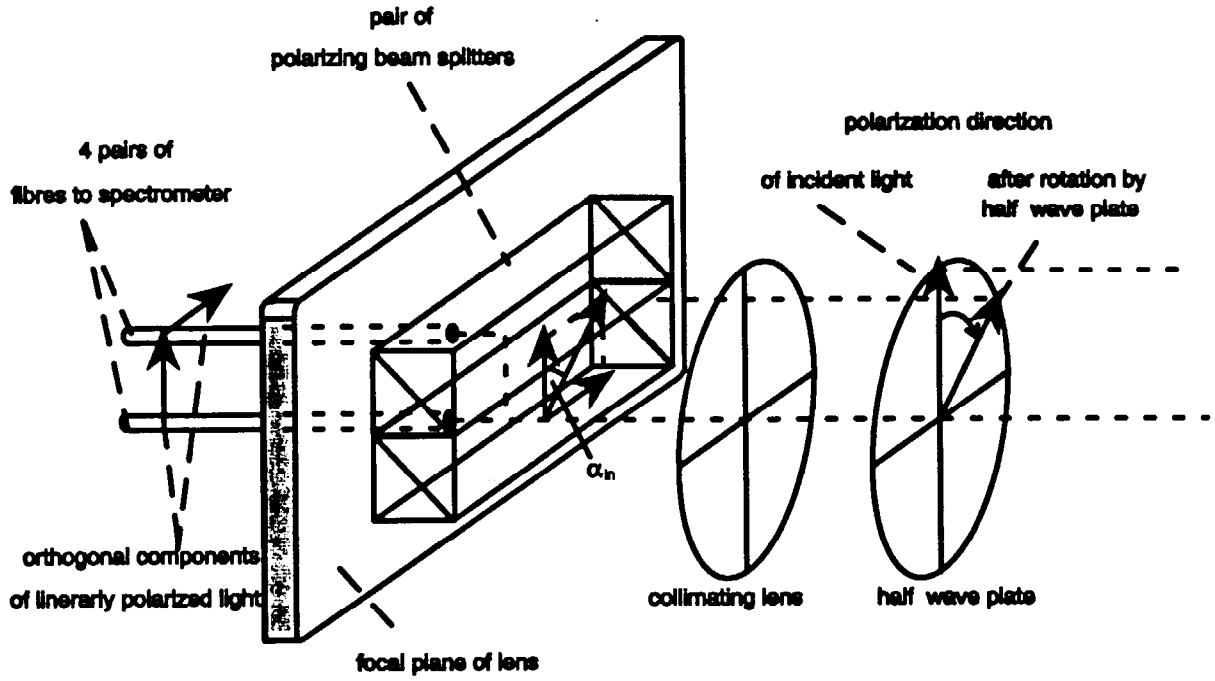

Fig.17 Measurement of the polarisation pattern in the Balmer-Alpha beam-emission spectrum. The light of each polarisation channel is spectrally resolved (cf. Fig.13) providing thus a simultaneous measurement of pitch angle and total magnetic field [45].

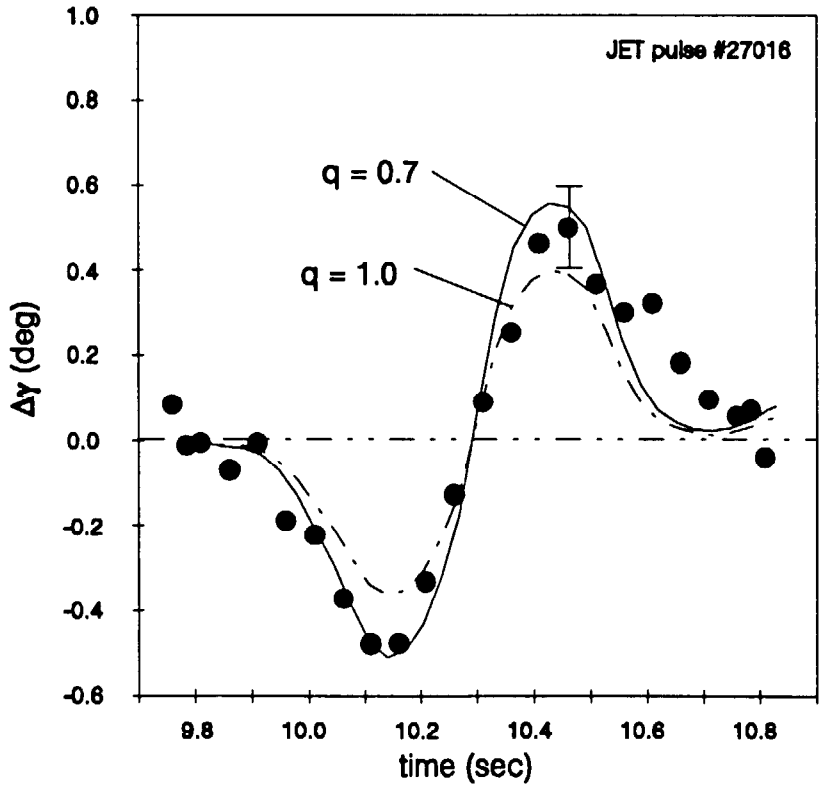

Fig.18 Change in the pitch angle of the magnetic field during a radial plasma sweep, inferred from the Stark effect measurement. Also shown are equilibrium calculations assuming a safety factor of either q=0.7 or q=1.0. The experimental data were smoothed over a 200 msec time period. The error bar indicates the uncertainty due to noise [27,45].

A powerful potential of the motional Stark technique is also the high precision Lorentz field strength measurement. The magnetic field and the beam velocity can be written in their respective poloidal, toroidal and normal components (B_n=0) leading to:

$$E_L = |v_{beam}| \sqrt{B_{pol}^2 + B_{tor}^2 - (\hat{v}_{pol} B_{pol} + \hat{v}_{tor} B_{tor})^2} \qquad (20)$$

which is related to the multiplet wavelength splitting by:

$$\Delta\lambda = \frac{3}{2} \frac{e a_0}{hc} \lambda_0^2 E_L \qquad (21)$$

where e, a_0, h and c have the usual meanings. Experimentally it is found that very small changes in the applied toroidal field are detectable by the changes in the Lorentz field. At the same time it can be inferred from equation (18) that, since $B_{pol} << B_{tor}$ close to the magnetic axis, for a constant B_{pol}, the Lorentz field strength can be used to determine the toroidal field nearby the magnetic axis. The statistical error of the wavelength splitting is less than 0.1%.

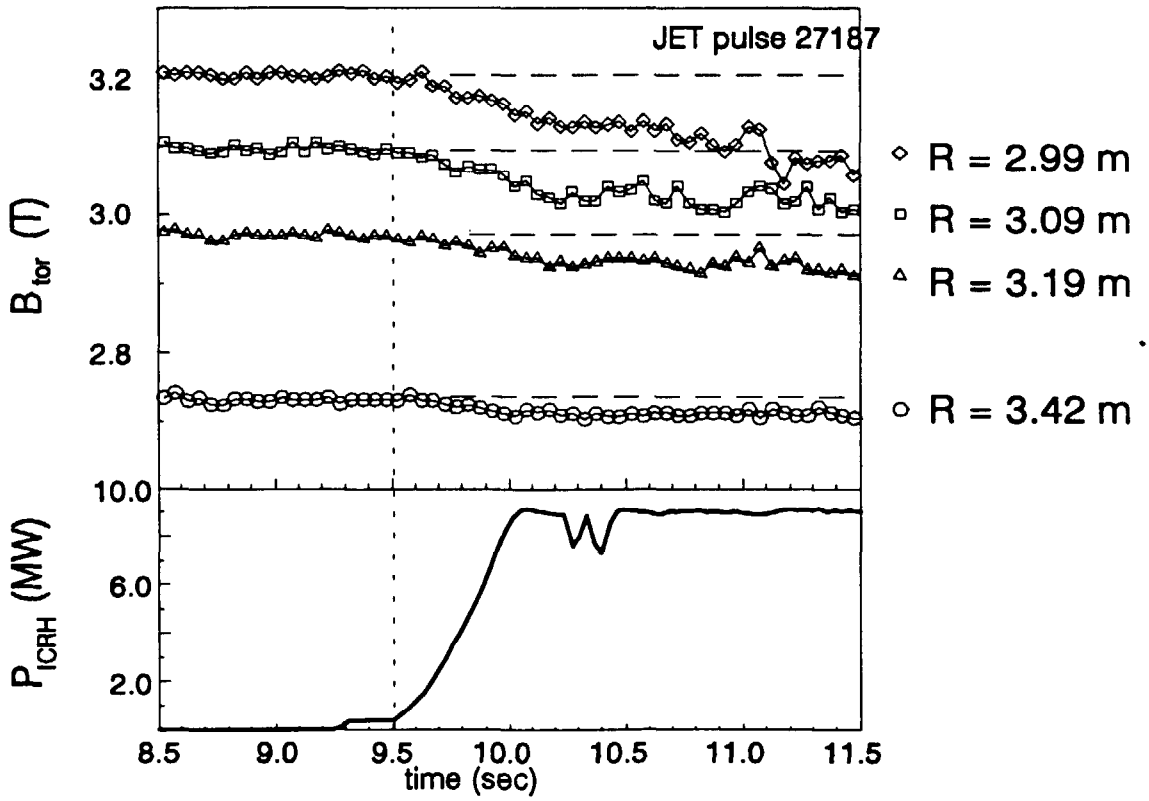

Fig.19 Observed correlation between toroidal field deduced from the Lorentz field strength **E=vxB** and total coupled ICRH power. The major radii of the 4 channels indicate that the greatest changes are nearby the ICRH resonance layer [45].

Diamagnetic effects caused by ICRH were observed for the first time by the motional Stark technique [24,45] and changes of the diamagnetic toroidal field of the order of 4% were established (Fig.19). The evolution of the thermal pressure (measured independently) and comparison with code simulation of the fast ion pressure indicates that the anisotropic population build up by fast particles is the dominant contribution to the diamagnetic effect in the plasma centre.

Alpha particle diagnostics

The main emphasis of the JET CX spectroscopy group in the case of alpha particle diagnostics has been the development of tools for the investigation of both slowing-down ($E < 150$ keV) and thermalised alpha particles ($E < 20$ keV). An important aspect has also been the attempt to establish links to other independent, quantitative diagnostics at the JET tokamak. A combination of atomic physics experiments and theoretical calculations has been initiated and co-ordinated by JET in order to provide the data required for the modelling of effective emission rates of the HeII(n=4 to n=3) transition. Fig.20 gives the result of dedicated atomic experiments and theoretical modelling leading to 'preferred' data curve [32]. Similar experimental and theoretical efforts are currently being carried out with neutral helium beam atoms acting as donors (cf. [17,46]).

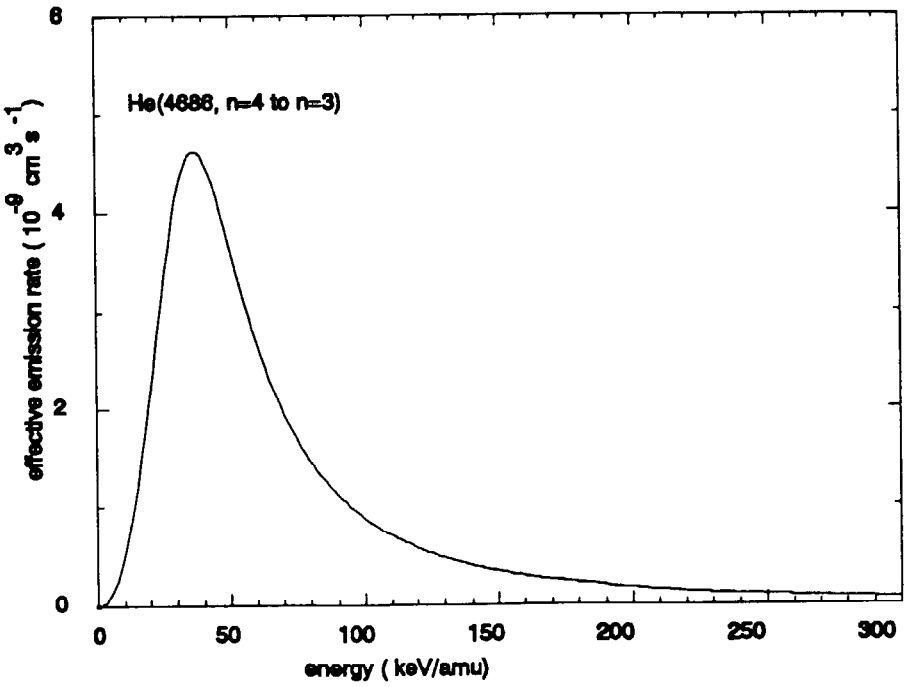

Fig.20 Effective emission rate coefficients for the HeII (n=4→3) transition. Crossed-beam experiments and atomic modelling have led to 'preferred' data (cf.[32]). The values are calculated for standard plasma conditions with T=3keV, $n_e=3\cdot10^{19}m^{-3}$, $Z_{eff}=2$.

The proper interpretation of spectra requires the unambiguous separation of the CX feature within a very complex set of HeII features at 4685Å (Fig.4) and then comparison of deduced ion temperatures to electron temperatures (Fig.21). The existence of the passive plasma edge CX feature can in principle affect the deduced core ion temperatures by an appreciable amount. Once the central feature is identified unambiguously by its temperature, for example in a high density plasma where we may assume equal electron and ion temperatures, an absolute density can be derived from its intensity. A number of independent tests, ranging from pure helium plasma calibration discharges to helium beam fuelling experiments with a known number of injected helium atoms have generally led to consistent results, confirming the validity of the atomic data and also of the analysis procedures.

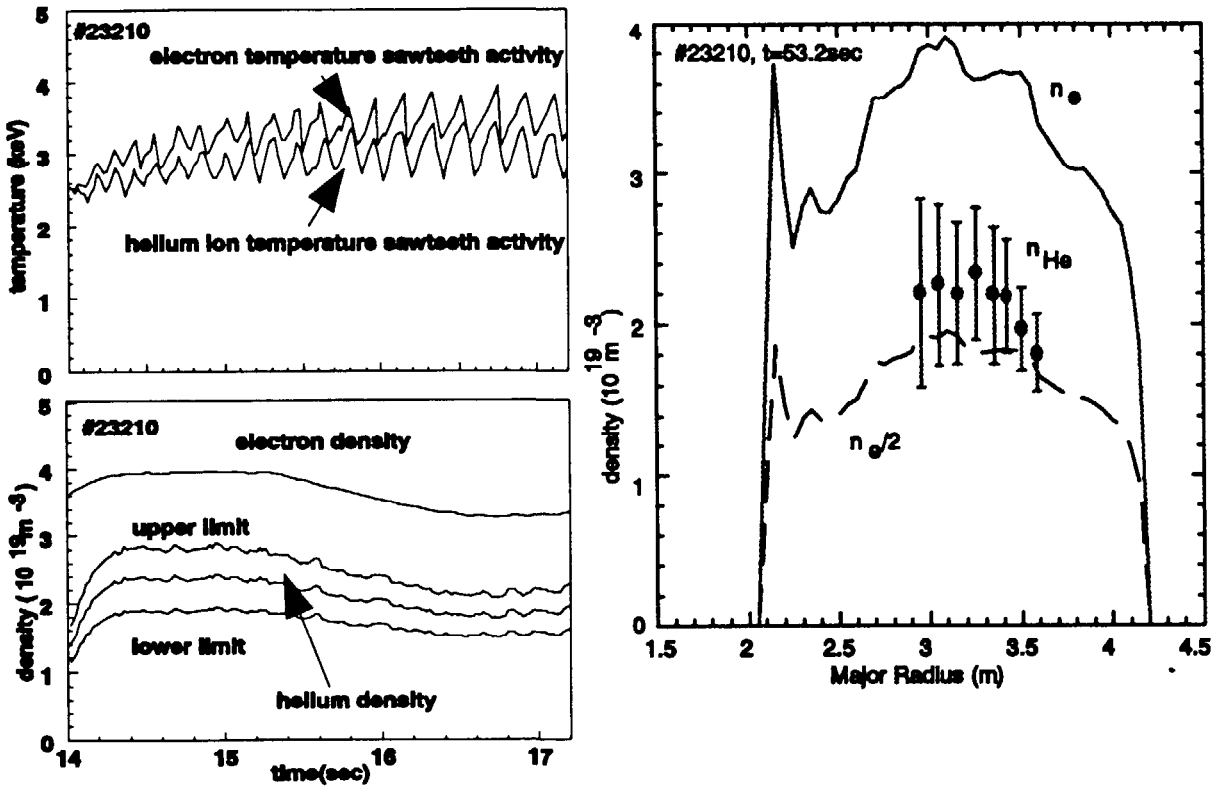

Fig. 21 Helium reference discharge with a) electron and ion temperature showing sawtooth oscillations, b) electron and helium density and c) radial profiles. Upper and lower values of the deduced helium density reflect attenuation- and statistical errors. The contributions of C and Be are negligible.

In JET neutral helium beam heating experiments (c.f. [43]) using $^3He^0$ beams with particle energies up to 145 keV, and neutral beam powers of up to 12 MW, distinctive broad band features were observed in the HeII 4685Å spectral range. Neutral beam injection leads to a population of fast ions with energies ranging from above thermal up to the injection energy. The distribution function of the fast particles is strongly anisotropic at the birth energy but subsequently isotropises in the course of the slowing-down process. For the description of the fast ion velocity distribution function an analytical solution of the neutral injection Fokker Planck equation is used (c.f. [47]) which gives the slowing-down distribution function as:

$$g_{slow}(v,\xi)=\frac{S\tau_s}{v^3+v_c^3}\frac{1}{\sqrt{4\pi\alpha}}\exp\{-\frac{(\xi-\xi_0)^2}{4\alpha}\} \qquad (22)$$

$$\alpha(v)=\frac{\beta}{3}(1-\xi_0^2)\log\frac{[1+(v_c/v)^3]}{[1+(v_c/v_b)^3]} \qquad (23)$$

where the initial angle between neutral beam and magnetic field is $\xi_0=\cos\psi_0$, v_b and v_c are the injection and critical velocity respectively, τ_S is the Spitzer slowing-down time, S is the beam deposition rate, $\beta=m_iZ_{eff}/2m$, where m_i, m are the plasma and beam ion mass respectively. The expected CX spectrum is calculated using the same procedure as in the thermal case (cf. equation (9)). The anisotropy of the distribution function is displayed by the two observation systems of JET, one perpendicular to the magnetic field and neutral beam line, and the second approximately parallel to the magnetic field and at an angle of 60° to the neutral beam line. Fig.22, Fig.23 and Fig.24 give a brief overview of characteristic results comparing predicted and observed spectra.

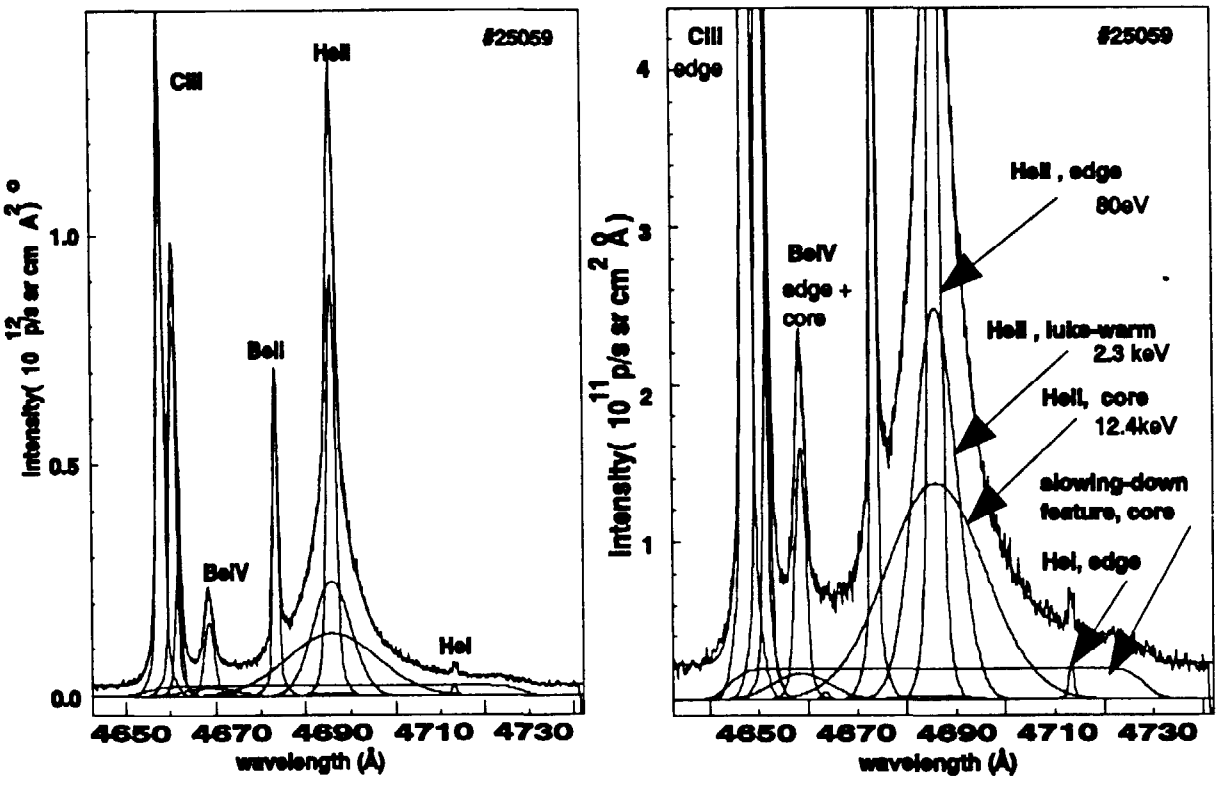

Fig.22 CXRS HeII spectrum during helium neutral beam heating a) overview, b) expanded spectrum, showing thermal and non-thermal components.

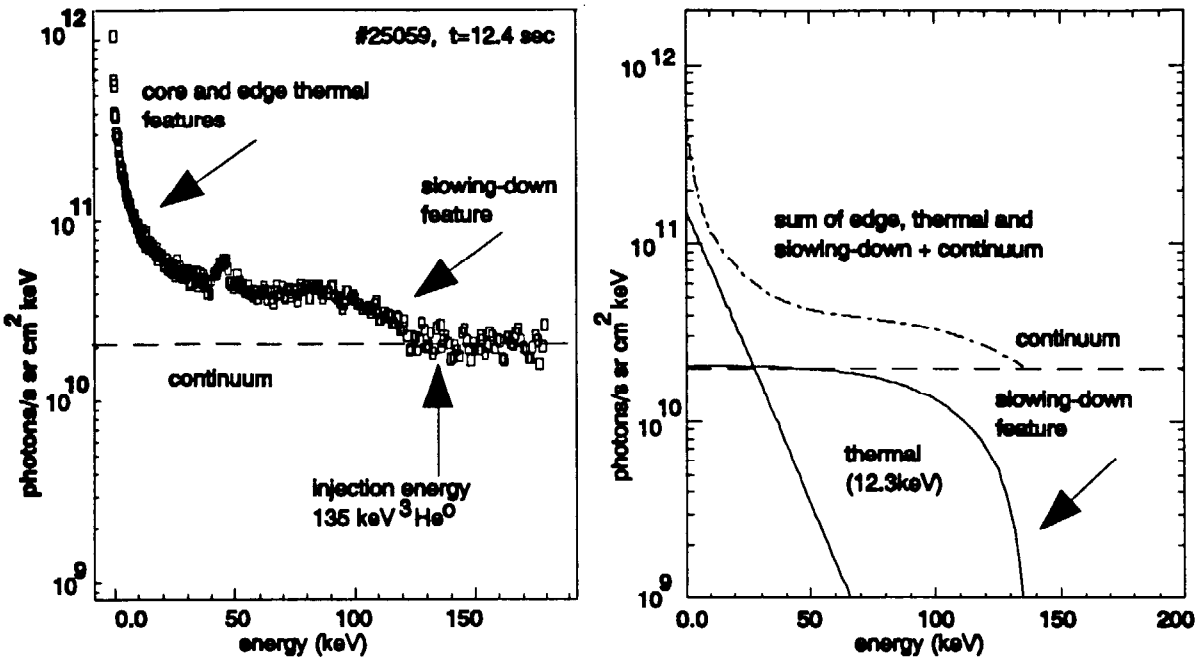

Fig.23 Logarithmic energy spectrum a) experimental b) prediction using slowing-down function equations (9,22) (cf.[33]).

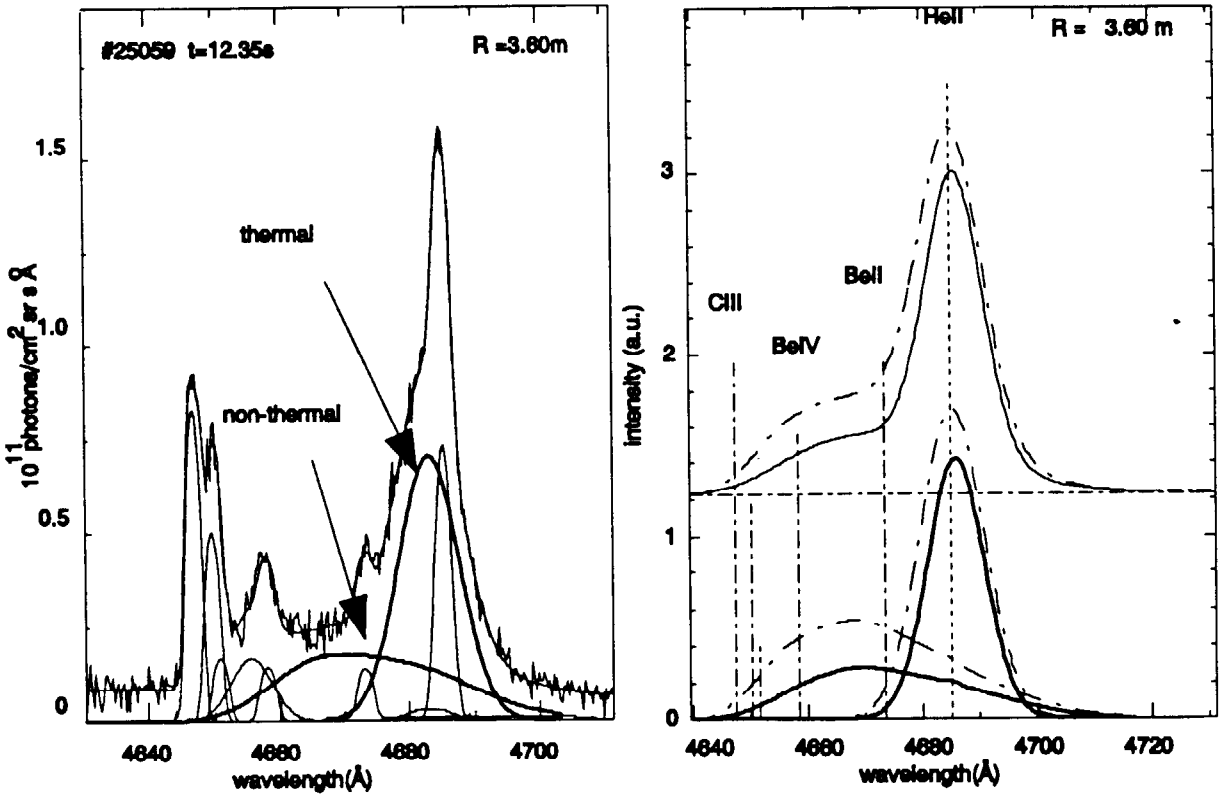

Fig.24 Simulated and experimental slowing-down spectra detected by the multi-chord system, with a viewing direction approximately parallel to the magnetic field and at 60° to the neutral beams (cf. [33]). The dashed lined spectra are calculated for constant emission rates and the solid lined spectra are based on the true collision energy dependent emission rate coefficients (cf. equations (9) and (22)).

Limiting factors for the quantitative use of CXRS

The two main limiting factors for a successful CX diagnostic depend primarily on the penetration of the neutral beam. The first is the *detection* of the active CX spectrum against the competing background spectrum and its noise level. The second factor, which is a more general constraint, is that for *quantitative use* of the derived spectra, to deduce absolute densities, the local neutral beam strength needs to be determined accurately. The beam strength n_b is calculated from fundamental atomic data such as stopping cross-sections (Fig.25) together with electron density and temperature profiles. An error in the input data of 10% implies that due to the exponential decay of the beam strength along the penetration path into the plasma, only a attenuation factor of $n_b/n_b(0) > 0.02$ can be tolerated. Beyond this level, attenuation errors, and therefore consequent errors in deduced alpha particle densities, exceed 30%.

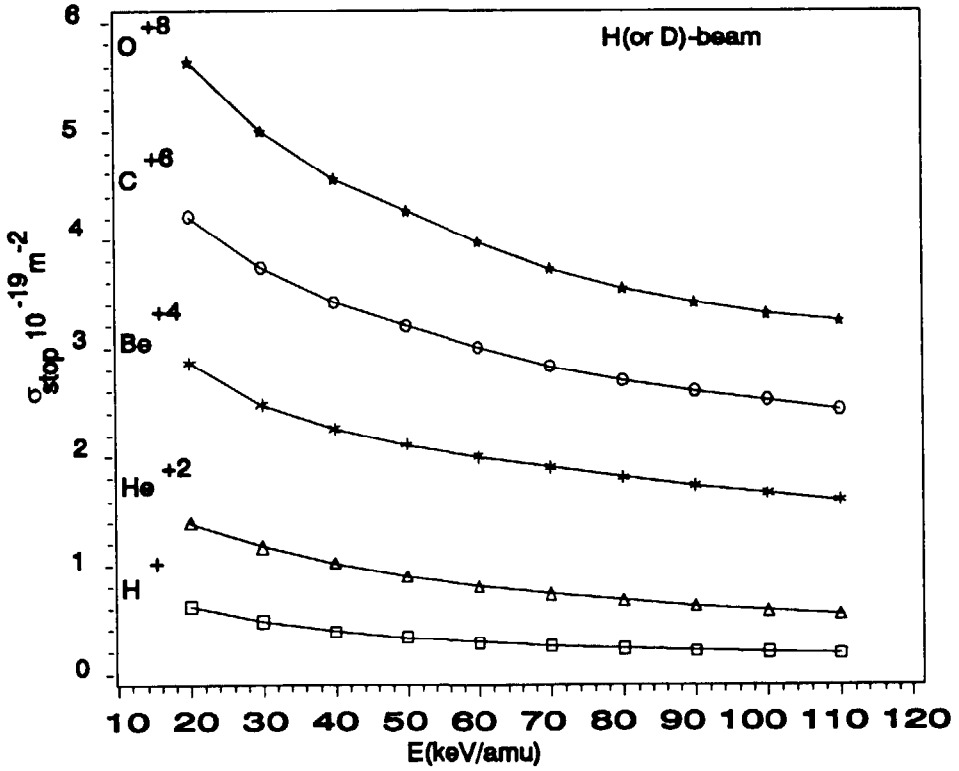

Fig.25 Total stopping cross-section for the case of neutral hydrogen (deuterium) beam acting as a probe beam for CXRS or BES diagnostic applications.

Typical impurity densities detected in JET plasmas vary between $5 \cdot 10^{16} m^{-3}$ (e.g. a low carbon content) and $5 \cdot 10^{19} m^{-3}$ (e.g. the helium density in a pure helium discharge). The lowest measurable density depends on a detection limit which is defined by the ability to extract a CX spectrum from a noisy background spectrum. The noise level may be defined by the ratio of measured count rate from charge exchange photons and of the count rate of fluctuations of the sum of background and CX signal. In the case of this detection limit, it is reasonable to assume

that the bremsstrahlung counts exceed those of the CX signal, $N_{brems} >> N_{CX}$, and the signal-to-noise is therefore :

$$\{\frac{S}{N}\} = \frac{N_{CX}}{\sqrt{N_{brems} + N_{CX}}} \approx \frac{N_{CX}}{\sqrt{N_{brems}}} \tag{24}$$

For the fluctuation level of the free-free continuum radiation background signal we have:

$$\tilde{N}^2 = B \cdot g_{ff} \cdot Z_{eff} < n_e^2(0) > L_p \frac{\Delta\lambda}{\lambda_{de}(0)} \Delta t \cdot \Re \tag{25}$$

Where $< n_e^2(0) > L_p$ is a line integrated equivalent of the electron density, Δt is the detection sampling time and $\Re$ the detector response. Separating all factors, which may be assumed to be constant, for example a constant impurity concentration and Z_{eff}, one obtains a signal-to-noise ratio, which is normalised to the neutral beam current I_n and other constant plasma parameters such as beam diameter $w_\perp$, concentration $c_z = n_z/n_e$, temperatures T_e and T_i respectively:

$$\{\frac{S}{N}\}^* = \{\frac{S}{N}\} \frac{w_\perp \cdot \sqrt{Z_{eff}}}{I_n \cdot c_z} \sqrt{\frac{v_i^2}{c \cdot v_e}} \sqrt{\frac{\lambda}{\Delta\lambda \Delta t \Re}} \tag{26}$$

$$\{\frac{S}{N}\}^* \propto \sigma_{CX}(E) \exp\{-\int dr n_e \sum_z c_z \sigma_{sz}(E)\}$$

The beam stopping cross-sections $\sigma_{S,Z}$ are primarily determined by the beam energy. Both charge exchange cross-sections and beam stopping cross-sections have only a small electron density dependence due to either redistribution or multiple step processes. For a given electron density there exists an optimum energy which is defined by a trade-off of gains from higher energies in beam penetration (Fig.25) but with losses at the same time from the drop of the CX emission rate (see also Fig. 6).

A further relevant consideration is the *quantitative* deduction of a local particle *density* from the measured CX photon flux. The error in the deduced density introduced by an error in the attenuation is given by (cf. equation (8)):

$$\frac{\Delta n_\alpha}{n_\alpha} = \frac{\Delta n_b}{n_b} \approx \frac{\Delta(\sigma_{s,z}, n_e)}{(\sigma_{s,z}, n_e)} \cdot \sum_z \sigma_{s,z} c_z \cdot \int dl \cdot n_e(l) \tag{27}$$

In the following example a total error of 10% error in electron density n_e and stopping cross-sections $\sigma_{S,Z}$ is assumed. In a plasma with an impurity ion composition of He^{2+}(10%), C^{6+}(2%), H^+(68%), that is an effective ion charge Z_{eff}=1.8, the sum $\Sigma\sigma_{s,z}c_z$ of all species contributing with their respective concentrations $c_z = n_z/n_e$ to the total stopping process is: $\Sigma\sigma_{s,z}c_z = 2.4 \cdot 10^{-20} m^2$. The individual values are: $\sigma_{s,H} = 1.9 \cdot 10^{-20} m^2$, $\sigma_{s,He} = 5.8 \cdot 10^{-20} m^2$ and $\sigma_{s,C} = 25.2 \cdot 10^{-20} m^2$. All cross-sections refer to a neutral hydrogen beam with 100keV/amu (cf. Fig.25). For a line integrated electron density of $<n_e L> = 2 \cdot 10^{20} m^2$, where the integration dl refers to the beam path between boundary and active CX volume, (this would correspond to

an observation in the core of the next-step fusion experiment ITER at a central density of $10^{20}m^{-3}$), the attenuation factor is $n_b/n_b(0)=e^{-4.8}=0.008$. The relative error in the calculated local beam density is therefore $\Delta n_b/n_b = 0.48$. At this error level the limits of quantitative use of CXRS are obviously reached, and even if a CX spectrum can be 'detected', its intensity can no longer be exploited reliably.

JET as an atomic oven

In the past years the instruments of the JET CXRS diagnostic have been used to establish some experimental ratios of CX emission rates. The deduction can be straight forward when two instruments share the same viewing line and hence the same beam geometry and bremsstrahlung level, but may be quite complex otherwise where the respective contributions from each beam and energy species to different viewing systems are difficult to assess. A further problem is the break-up in the contributions of the three energy species (cf. equation (5)). Usually only in the plasma centre where the full energy component dominates it is justified to establish experimental ratios with some confidence. Table II shows that experimental results are nonetheless within 30% of modelled predictions (cf. [19, 29,48]).

The weak higher n-shell transitions (e.g. CVI n=11→8) are usually also hard to extract unambiguously from complex spectra. Beam modulation, i.e. comparison of two subsequent time slices where the neutral beams are switched on and off, has given clear ratios for the two BeIV CX line observed within the same spectral range (Fig.26). The experimental results of the emission rate ratio $\sigma_{CX}(n=6\rightarrow5)$: $\sigma_{CX}(n=8\rightarrow6)$ have in this case even initiated further atomic modelling efforts [29].

Table II gives an overview of results achieved by the CX instruments monitoring visible and UV CXRS lines [48].

table II

ion	transitions	wavelengths	neutral beam	experiment (JET)		modelling	
C^{5+}	σ(10-8)/σ(8-7)	4449Å/5290Å	D^0 @40keV/amu	0.15	[19]	0.11	[11,17]
C^{5+}	σ(7-6)/σ(11-8)	3434Å/3438Å	D^0 @70keV/amu	22.2±3.8	[48]	27.5	[11,17]
C^{5+}	σ(7-6)/σ(11-8)	3434Å/3438Å	D^0 @37keV/amu	30.1±8.1	[48]	43.0	[11,17]
C^{5+}	σ(7-6)/σ(8-7)	3434Å/5290Å	D^0 @70keV/amu	2.72±0.2	[48]	2.55	[11,17]
O^{7+}	σ(10-9)/σ(9-8)	6068Å/4340Å	D^0 @40keV/amu	0.42	[19]	0.45	[11,17]
Be^{3+}	σ(6-5)/σ(8-6)	4658Å/4685Å	D^0 @40keV/amu	5.5±0.5	[29]	5.2	[29]
Be^{3+}	σ(5-4)/σ(6-5)	2530Å/4658Å	D^0 @65keV/amu	4.0±0.3	[48]	3.2	[29]
He^+	σ(5-3)/σ(4-3)	3203Å/4685Å	He^0@43keV/amu	0.29±0.05	[48]	0.32	[32]

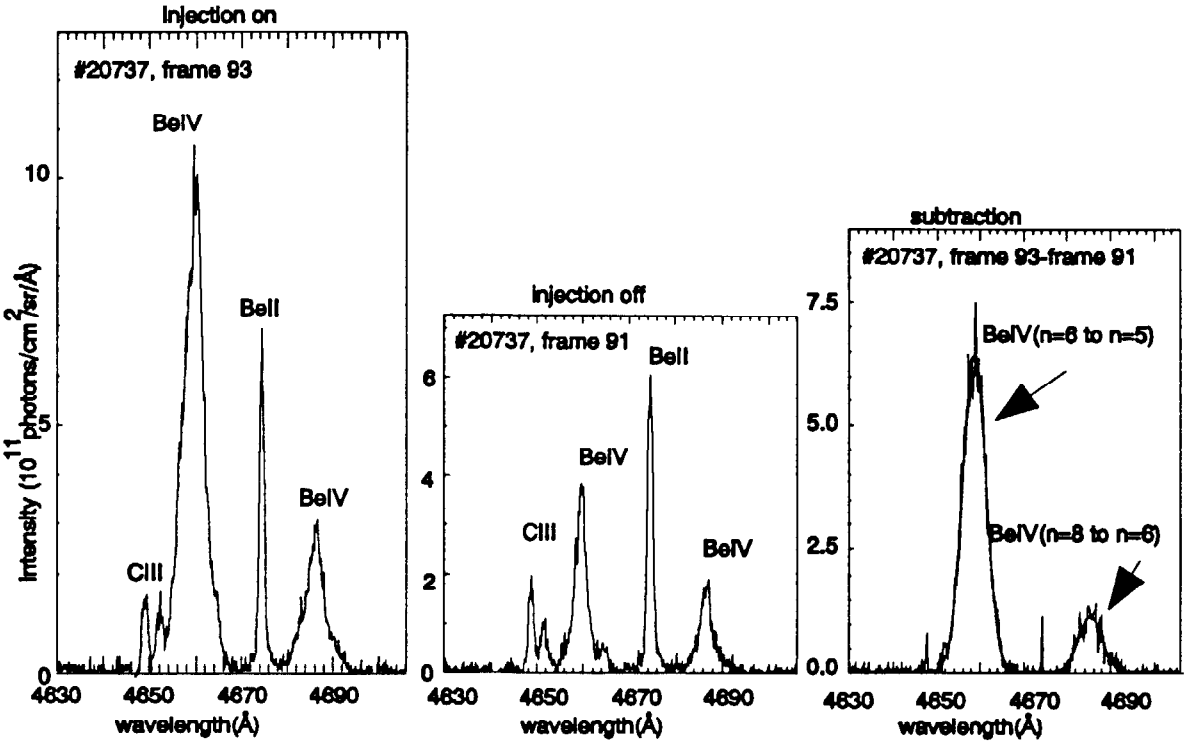

Fig.26 Beam modulation experiment showing active and passive emission spectra of BeIV, BeII and CIV. The plasma is a high density plasma leaning against a beryllium tiled belt-limiter and Be is the dominant impurity [29].

Summary and Conclusions

Many of the objectives of active beam spectroscopy have been successfully addressed in the last decade and a substantial effort has occurred to establish atomic data required for a quantitative interpretation of CXRS spectra measured in fusion devices. The atomic modelling of spectra, parametric description of spectral shapes, and comparison with experimental results has advanced considerably and has been successfully tested for most of the dominant low-Z impurity CX spectra. A number of independent bench-mark tests have verified the quantitative capability of charge exchange spectroscopy. Absolute impurity densities can be measured locally and temporally resolved. The overall uncertainty is at present approximately 30%, with neutral beam stopping and related processes playing a decisive role in the reliability of deduced density levels.

The mechanism of collision energy dependent emission rates on observed CX spectra is understood and analytical and numerical procedures for the deduction of temperatures, velocities and effective rates have been developed for thermal velocity distribution functions. Non-thermal slowing-down functions and anisotropic CX spectra observed in helium beam fuelling experiments need further modelling and development of comprehensive distribution functions.

The analysis of radial impurity profiles, the deduction of transport coefficients from local gradients, in particular in the case of thermal alpha particles, is still an outstanding problem and requires further efforts.
Beam emission spectroscopy promises to be a attractive diagnostic tool, and it will probably become a routine diagnostic technique in the near future. The quantitative restrictions imposed by the calculation of beam attenuation processes for CXRS can possibly be facilitated by complementary inputs from BES. Plasma density fluctuation measurements based on BES are currently being investigated on other fusion devices.
Magnetic field studies based on the motional Stark effect have demonstrated their potential in precise local measurements. This refers in particular to a combined measurement of the Stark polarisation pattern and Lorentz field strength. Low frequency sawtooth oscillations of the toroidal field are resolvable, but high frequency magnetic field fluctuations appear to be beyond the scope of existing JET experimental capabilities.
Helium neutral beams will play a greater role in future next-step fusion devices due to their lower stopping cross-sections. Beam emission spectroscopy on neutral helium beams is however still in its infancy and requires further experimental data and further modelling efforts. Multiple-step processes and the relevance of metastable populations in helium neutral beams are the subject of theoretical and experimental studies.
Low-energy charge exchange excitation processes will represent a dominant factor in the interpretation of plasma edge physics and for the diagnosis of low-Z impurities in the divertor chamber.

Acknowledgement

The progress of active beam spectroscopy at JET has greatly benefited from the support by Drs W. Engelhardt (now IPP Garching), P.R. Thomas and M. Keilhacker who have encouraged continuously new developments and also helped to strengthen the links to the atomic physics community. The paper is the result of numerous contributions by the members of the JET Charge Exchange Spectroscopy Group as indicated by the list of references. Critical comments and stimulating discussions with many members of the JET team, highlighting the needs for quantitative CXRS results, have also helped to re-define and adjust the scope of active beam spectroscopy in the course of the last years.

References:

1 Rebut P.H. and the JET team (1992) Nuclear Fusion, **32**, 187
2 Isler R.C., Phys.Rev.Lett. **38**, 1359(1977)
3 Afrosimov V.V., Gordeev Y.S., Zinoviev A.N., Korotkov A.A., JETP Lett.**28**, 501(1979)
4 Isler R.C., Murray L.E., Appl. Phys. Lett. **42**, 355(1983)
5 Fonck R.J., Goldston R.J., Kaita R., Post D., Appl. Phys. Lett. **42**,239(1983)
6 Groebner R.J., Brooks N.H., Burrell K.H., Rottler L., Appl.Phys. Lett. **43**,920(1983)
7 Fonck R.J, Darrow D.S., Jaehnig et al., Phys.Rev. (1984) **29**,3288
8 Hawkes N.C., Peacock N.J. Nuclear Fusion **25**,971(1985)
9 TFR Group, Phys.Lett. **122A**,29(1985)

10 Carolan P.G., Duval B.P., Field A.R. Phys.Rev. A35,3454(1987)
11 Boileau A., von Hellermann M., Horton L.D., Spence J., Summers H.P. (1989) Plasma Phys. Contr. Fusion **31**,779
12 Boileau A., von Hellermann M., Horton L.D., Summers H.P., Morgan P.D. (1989) Nuclear Fusion **29**,1449
13 Weisen H., von Hellermann M., Boileau A., Horton L.D., Mandl W., Summers H.P. (1989) Nuclear Fusion, **29**, 2187
14 von Hellermann M., Mandl W., Summers H., Weisen H., Boileau A., Morgan P.D., Morsi H., König R.T.W., Stamp M.F., Wolf R.C. (1990) Rev. Sci. Instr.**61**,3479
15 von Hellermann M. and Summers H.P. (1992), Rev. Sci. Instr. **63**, 5132
16 Boley C.D., Janev R.K., Post D.E. (1984), Phys.Rev.Letters, **52**, 534
17 Summers H.P., von Hellermann M.G., de Heer F.J., Hoekstra R., (1992) Nuclear Fusion Supplement **3**, 7
18 Korotkov A.A (1992) Nuclear Fusion Supplement **3**, 79
19 Boileau A., PhD thesis, Université du Québec (1988), 'Etude des éléments légers complètement ionisés dans le tokamak JET par observation spectroscopique de la réaction d'échange de charge'
20 Boileau A., von Hellermann M., Mandl W., Summers H.P., Weisen H., Zinoviev A. (1989) J.Phys.B At. Mol.Opt. Phys. **22**,L145
21 Fonck R.J., (1990) Rev.Sci. Instr. **61**,3070
22 Durst D., Fonck R.J., Cosby B., Evensen H., (1992) Rev.Sci. Instr.,63,4907
23 Mandl W., PhD Thesis, University of Munich 1991, JET-IR(92)**05**, 'Development of active Balmer-Alpha spectroscopy at JET'
24 Mandl W., Wolf R.C., von Hellermann M., Summers H.P., submitted to Plasma Physics and Contr. Fusion, JET-P(92)**93**
25 Levinton F.M., Fonck R.J., Gammel G.M., Kaita R., Kugel H.W., Powell E.T., Roberts D.W.(1989), Phys.Rev.Lett. **63**,2060
26 Wroblewski D., Burrell K.H., Lao L.L., Politzer P., West W.P.(1990), Rev.Sci.Instr.**61**,3552
27 Wolf R.C., O'Rourke J., Edwards A.W., von Hellermann M. JET-P(92)99, accepted by Nuclear Fusion (1993)
28 Weisen H., Bergsaker H., Campbell D.J., Erents S.K., de Kock L.C., McCracken G.M. Stamp M.F., Summers D.R., Thomas P.R., von Hellermann M., Zhu. J. (1991) Nuclear Fusion, **31**, 2247
29 Summers H.P., Dickson W., Boileau A., Burke B.G., Denne-Hinnov B., Fritsch W., Giannella R., Hawkes N.C., von Hellermann M., Mandl W., Peacock N.J., Reid R., Stamp M.F., Thomas P.R. (1991) Plasma Phys.Contr.Fusion **34**,325
30 Post D.G., 'International Workshop on Helium Transport and Exhaust' (1991) Nuclear Fusion, **31**,2181, Editor J.Hogan, D.Hillis
31 Young K.M. (1992), Plasma Phys. Contr. Fusion, **34**, 2001
32 von Hellermann M., Mandl W., Summers H.P., Boileau A., Hoekstra R., de Heer F., Frieling J. (1991) Plasma Phys.Contr.Fusion, **33**,1805
33 von Hellermann M., Core W.G.F., Frieling J., Horton L.D., Mandl W., Summers H.P. accepted for publication by Plasma Phys.Contr.Fusion (1993), JET-P(92)**95**
34 Frieling G.J., PhD Thesis, University of Utrecht 1993, 'Charge exchange spectroscopy for

α-particle diagnostics in the Joint European Torus'
35 Morsi H.M. et al., Proc. 18 European Conf. Contr. Fus. Plasma Physics, 1991, Berlin, JET-P(91)**08**
36 Bishop C.M., Roach C., von Hellermann M., accepted for publication by Plasma Phys. Contr. Fusion (1993), JET-P(92)90
37 Howell R.B., Fonck R.J., Knize R.T., Jaehnig K.P. (1988) Rev.Sci.Instr.**59**,1521
38 von Hellermann M.G., Boileau A., Horton L.D., Summers H.P., 14th European Conf.on Contr. Fus. and Plasma Heating Madrid, June 87, JET- P(87)**23**,189
39 Danielsson M., von Hellermann M.G., Kallne E., Mandl W., Morsi H., Summers H.P., Zastrow K.D ,Rev.Sci.Instr.(1992),**63**, 2241
40 von Hellermann M., Breger P., Frieling J., König R., Summers H.P., 'Analytical Approximation of Cross-Section Effects on CX Spectra', to be submitted to Rev. Sci. Instr.(1993)
41 Balet B., Stubberfield P.M., Cordey J.G., Deliyanakis N., Greenfield C.M., Jones T.T.C., König R., Marcus F., Nave M.F., O'Brien D.P., Sadler G., Thomsen K., von Hellermann M., 'Particle and Energy Transport during the First Tritium Experiments on JET', to be published (1993)
42 Asher, Perez J.Appl.Phys.(1979)**50**,5569
43 Adams J.M., Jarvis O.N., Sadler G.J., Syme D.B., Watkins N. accepted by Nucl.Instr.&Meth. (1993)JET-P(92)**27**
44 Marcus F. et al. (1992), Plasma Phys. Contr. Fus.,**34**, 1371
45 Wolf R.C., PhD thesis, Universität Düsseldorf 1993, 'Measurement of the local magnetic field inside a tokamak plasma (JET) by means of the motional Stark effect and analysis of the internal magnetic field structure and dynamics', to appear as JET report (1993)
46 Hoekstra R., Summers H.P., F. de Heer, (1992) Nuclear Fusion suppl. **3**,63
47 Core W.G.F. (1992), JET-R(92)**11**
48 Schröpf H., MSc-Thesis, Technische Universität München 1992, 'Analyse von Ladungsaustauschspektren im Ultravioletten am Fusionspexperiment JET', Morsi H., Schröpf H., König R., von Hellermann M., ' Results of CXRS UV-spectroscopy at JET', to be published